
ON THE ROBUSTNESS OF FULLY-SPIKING NEURAL NETWORKS IN OPEN-WORLD SCENARIOS USING FORWARD-ONLY LEARNING ALGORITHMS

Erik B. Terres-Escudero
DeustoTech
University of Deusto
48014 Bilbao, Bizkaia, Spain
e.terres@deusto.es

Javier Del Ser, Aitor Martínez-Seras
TECNALIA
48160 Derio, Bizkaia, Spain
javier.delser@tecnalia.com
aitor.martinez@tecnalia.com

Pablo Garcia-Bringas
DeustoTech
University of Deusto
48014 Bilbo, Bizkaia, Spain
pablo.garcia.bringas@deusto.es

ABSTRACT

In the last decade, Artificial Intelligence (AI) models have rapidly integrated into production pipelines propelled by their excellent modeling performance. However, the development of these models has not been matched by advancements in algorithms ensuring their safety, failing to guarantee robust behavior against Out-of-Distribution (OoD) inputs outside their learning domain. Furthermore, there is a growing concern with the sustainability of AI models and their required energy consumption in both training and inference phases. To mitigate these issues, this work explores the use of the Forward-Forward Algorithm (FFA), a biologically plausible alternative to the Backpropagation algorithm, adapted to the spiking domain to enhance the overall energy efficiency of the model. By capitalizing on the highly expressive topology emerging from the latent space of models trained with FFA, we develop a novel FF-SCP algorithm for OoD Detection. Our approach measures the likelihood of a sample belonging to the in-distribution (ID) data by using the distance from the latent representation of samples to class-representative manifolds. Additionally, to provide deeper insights into our OoD pipeline, we propose a gradient-free attribution technique that highlights the features of a sample pushing it away from the distribution of any class. Multiple experiments using our spiking FFA adaptation demonstrate that the achieved accuracy levels are comparable to those seen in analog networks trained via back-propagation. Furthermore, OoD detection experiments on multiple datasets (e.g., Omniglot and Not-MNIST) prove that FF-SCP outperforms avant-garde OoD detectors within the spiking domain in terms of several metrics used in this area, including AUROC, AUPR, and FPR-95. We also present a qualitative analysis of our explainability technique, exposing the precision by which the method detects OoD features, such as embedded artifacts or missing regions, in multiple instances of MNIST and KMNIST. Our results underscore the enhanced robustness that can be achieved by analyzing the latent spaces produced by already trained models.

Keywords Forward-Forward Algorithm · Forward-Only Learning · Spiking Neural Networks · Out-of-Distribution Detection · Explainable Artificial Intelligence

1 Introduction

The fast development of learning algorithms has drastically impacted our dependency on Artificial Intelligence (AI) models, as their exceptional capabilities have led to their continual integration into production-ready software. However, this rapid pace has not been accompanied by additional safety guarantees to address well-known issues faced by modern AI systems. Among these shortcomings, the lack of robustness against inputs outside the training distribution poses a significant challenge in ensuring functionality in scenarios where generalization capabilities are essential [1]. Consequently, many people are hesitant to rely on AI for critical decisions in fields such as medicine or law, even if the model's performance surpasses that of human experts on specific tasks [2]. This limitation on the generalization capability arises from the predominant use of gradient Back-Propagation (BP) for training models within the AI field.

Although these models demonstrate excellent performance across a wide range of tasks, their tendency to overfit on training data and their inadequate responses to novel inputs make them highly unreliable tools for achieving high robustness standards.

Motivated by the learning capabilities of the brain, a novel biologically plausible learning heuristic denoted as the Forward-Forward Algorithm (FFA) was recently introduced by Hinton [3], which has showcased competitive accuracy when compared with BP. However, its most promising property lies within its latent space, which provides fundamental characteristics required for developing robust models. As multiple authors have observed since then [4, 5], the emerging latent space of this algorithm is characterized by classes residing tightly packed together in small clusters, while remaining distinct from other classes. Having tight compression of the data is pivotal in ensuring that models behave correctly when presented with data outside the training distribution, as the latent vector representation would lie outside any of the clusters identified from the training latent space. This property is crucial for ensuring a correct behavior with data from training datasets, as samples outside these clusters can be quickly identified as not belonging to the training distribution. Although the algorithm was initially presented as a biologically plausible alternative, most implementations have relied on analog neural models, leading to reduced research on their spiking counterparts. However, the set of papers working on spiking adaptations have shown how FFA can achieve competitive accuracy levels [6], paving the way for further neuromorphic implementations that promise faster and more energy efficient alternatives.

This work presents a seamless integration of FFA into Spiking Neural Networks (SNNs) via surrogate gradients to fully leverage the internal properties of spiking models. By capitalizing on their characteristic latent space, we create a novel Out-of-Distribution (OoD) Detection Algorithm that uses the latent distance between a sample and the set of In-Distribution (ID) clusters to determine whether a sample should be labeled as either OoD or ID. To extend the functionality of this algorithm, we have developed an interpretability technique that can generate an attribution map for a specific input instance with respect to any arbitrary class, highlighting features that do not correspond with those expected from the distribution of the desired class. This algorithm eases the task of detecting possible artifacts that could be affecting the model’s decision among samples labeled as OoD. Our results showcase the enhanced OoD detection accuracy in spiking networks when employing FFA, demonstrating that its enhanced representational properties improve the robustness of the models. Furthermore, our attribution method proves effective in detecting key features that push a data sample from its respective class towards OoD regions.

The rest of this paper is structured as follows: Section 2 provides a comprehensive review of related work. Section 3 elaborates on all the methodological approaches developed in this work. Specifically, Subsection 3.1 presents the approach taken to adapt FFA for SNNs, Subsection 3.2 describes the FF-SCP algorithm, and Subsection 3.3 introduces our attribution algorithm. Next, Section 4 presents the research questions that this work addresses, along with the experimental setup used for the experiments. Subsequently, Section 5 presents the experimental results, along with a discussion on the observed limitations. Finally, Section 6 outlines the conclusions of the paper and delineates directions for future research.

2 Related Work and Contributions

In this section, we present a comprehensive overview of relevant literature for this work, focusing on the following central topics: Spiking Neural Networks (Subsection 2.1); Forward-only Learning Algorithms (Subsection 2.2); Out-of-Distribution Detection (Subsection 2.3); and Explainability and Attribution (Subsection 2.4). Finally, Subsection 2.5 details the contribution that this papers offer with respect to the current literature.

2.1 Spiking Neural Networks

SNNs constitute a special category of artificial neural networks inspired by biological models, aiming to replicate the communication patterns found in real neurons within the brain. Unlike traditional approaches, primarily driven by Analog Neural Networks (ANNs) that rely on continuous activation values to forward information, spiking models operate by using discrete pulses of information, known as *spikes*. The internal dynamics of the neuron, determined by the chosen neural model, dictate when spikes occur and are typically presented as a dynamical system that provides a mathematical approximation of the behavior observed in real neurons [7]. Consequently, neurons can exhibit highly complex dynamics depending on the neural model, the degree of biological plausibility and the total computational complexity desired for the simulation.

In this work, we rely on the Leaky Integrate-and-Fire (LIF) neural model, known for preserving the standard action-potential dynamic while achieving high computational efficiency [8, 9]. Under this model, the membrane potential U of the neuron is tracked and updated in response to the external stimuli I_{in} , which represents the information forwarded to the neuron via the axon. Whenever the membrane potential reaches a threshold θ_{thr} , a spike is generated and forwarded

to subsequent neurons, at which point the membrane potential is reset to zero. To prevent unbounded activity, a constant decay τ is applied, exponentially reducing the membrane potential over time. Under a discrete time formulation, the neuron’s membrane potential $U(t)$ is updated as follows:

$$U(t) = \tau \cdot U(t - 1) + R \cdot I_{\text{in}}(t), \quad (1)$$

where $U(t - 1)$ represents the membrane potential at the previous time step, and R is a scaling factor of the input. Once $U(t)$ is computed, the value of the output spike $S(t)$ is determined by the activity of the membrane:

$$S(t) = \mathbb{I}(U(t) > \theta_{\text{thr}}), \quad (2)$$

$$U(t) = U(t) \cdot (1 - S(t)), \quad (3)$$

where $\mathbb{I}(\cdot)$ is an auxiliary binary function taking value 1 if its argument is true (0 otherwise).

By relying on these models, the neuromorphic computing field has been a highly active area due to the energy and speed advantages they offer, demonstrating proficiency in multiple artificial intelligence tasks. In the field of Computer Vision, deep spiking neural networks have been effectively employed for image classification [10] and image detection tasks [11]. In the Natural Language Processing domain, Zhu et al. implemented a fully spiking version of a Large Language Model, demonstrating its competitiveness against analog language models such as GPT-2 [12]. Additionally, notable advantages have been observed in a brain-like navigation systems by utilizing LIF neurons trained by Spike-Timing-Dependent Plasticity (STDP), a biologically plausible learning rule [13].

2.2 Forward-only Learning Algorithms

BP stands as the most commonly employed algorithm for training artificial neural networks. This method computes exact gradient values of the weights with respect to a loss function by back-propagating the error from the output through the layers using the chain rule. Due to the precision of weight updates, BP has achieved state-of-the-art results in terms of accuracy across a multitude of tasks. However, the requirement for differentiability in the functions defining the network poses a clear limitation for non-differentiable neural models, such as those in spiking systems. To address this limitation, the most commonly employed approach involves replacing the neural model with a differentiable approximation so that the backward pass can create a faithful approximation of the gradients [14]. Additionally, due to the optimization nature of the problem, models trained with BP have been observed to be prone to overfitting [15], consequently failing to generalize beyond the training distribution and resulting in unknown outcomes when presented with new, unseen data.

To overcome the present limitations of BP, the NeuroAI field has recently emerged as a strong alternative movement. This field advocates for incorporating and studying learning mechanisms observed in the brain to improve current models, aiming for fast learning and highly robust learning models [16]. Among these approaches, the branch of forward-only algorithms poses a viable method for bridging the gap between neuroscience and AI by focusing on a reduced set of biological properties while preserving the advantage of being computationally efficient and staying close to traditional AI methods. These algorithms specifically address the weight transport and update lock problems by relying solely on forward passes. By avoiding these biological incompatibilities, these algorithms also enhance integrability into neuromorphic systems, which are better suited for spiking models.

Recently, the Forward-Forward Algorithm was introduced as a novel forward-only alternative to BP, advocating for a biologically motivated heuristic in which the backward pass is replaced by an additional contrastive forward pass [3]. In this secondary pass, the model is presented with an adversarial sample to contrastively learn to distinguish between samples from the training set (referred to as *positive* or D_{\oplus}) and synthetically created data (referred to as *negative* or D_{\ominus}). As it follows from its forward-only nature, each layer is trained independently, using a layer-specific loss function that relies solely on local information. To formulate this loss function, Hinton proposed the use of a *goodness score*, which measures the likelihood of a latent vector from belonging to the positive data distribution. This goodness function $G : \mathbb{L} \rightarrow \mathbb{R}$ is defined as the squared Euclidean distance of the latent vector from its original position, where \mathbb{L} denotes the latent space of the given layer. This choice was motivated by the simplicity of its derivative, which facilitates clear and effective weight update expressions. Under this formulation, the goodness score serves as a measure of the layer’s activity, advocating for achieving highly active layers when presented with positive samples, and nearly dormant outputs when encountering a negative instance.

To avoid relying on a regression-based task, which could provoke unstable learning dynamics, a probability-based approach was taken. By using the Binary Cross-Entropy loss with a probability function defined over the goodness scores, the approach ensures a balanced distribution of positive and negative activities. The probability function $P : \mathbb{R} \rightarrow [0, 1]$ is chosen to map the goodness scores to a final probability estimation, indicating the likelihood of a latent vector being obtained from a sample from the positive data distribution. This function is defined by the logistic

function, modulated by a threshold value θ to shift the scores toward zero when presented with near-zero goodness scores. The formal expression for this function is given by $P(x; \theta) = \text{sigmoid}(x - \theta)$.

As previously stated, each learning step involves two contrastive forward passes: a positive pass, where each layer is presented with a sample from the training distribution and optimized to maximize its goodness score; and a negative pass, where a synthetic sample is employed to teach the model to remain dormant when presented with non-training data. In its supervised formulation, positive instances are created by embedding a one-hot encoding vector of the corresponding label into the corner of the base input image. Analogously, negative data is created by taking a sample from the training dataset and embedding a random label that does not align with its corresponding one. Using this positive and negative generation method, the inference process is achieved by computing the goodness score of the data sample with respect to all labels, thereby selecting the label achieving the highest score as the output class. In a subsequent work, Lee et al. proposed a refinement of this method by using random binary vectors associated with each class, which were then appended to the end of the vector of the data sample, reducing the overlap between the data and the label, and resulting in improved classification accuracy [17].

The algorithm has gained significant attention from NeuroAI researchers, leading to multiple improvements over the original formulations, which have resulted in increased accuracy [18, 17] and improved biological plausibility [5, 6]. Expanding on the latter topic, Ororbria and Mali pioneered additional biological heuristics for FFA by integrating predictive coding, which allows the model to provide accurate reconstructions of the latent space [5]. Simultaneously, Ororbria proposed the first implementation of an event-driven version of FFA, replacing the conventional error-driven update with modulated Hebbian learning rules, demonstrating a straightforward adaptation of FFA into a biologically plausible spiking learning pipeline [6]. Both of these works, along with [4] and [19], have presented consistent results showcasing the representational properties that emerge from this algorithm. Their work highlights the particular latent topology that results after training, characterized by sparse latent activation and neural specialization that leads to several compact clusters comprised of instances of the same class, which lie far from each other, rendering class clusters highly separated within the space.

2.3 Out-of-Distribution Detection

OoD detection is a crucial task for developing production-ready software, as it ensures that models are not presented with inputs outside their training distribution, which could result in unpredictable and potentially dangerous outputs [1]. To achieve this, OoD detection algorithms define a scoring function that measures the likelihood of a sample from belonging to the ID dataset, which is then used to label input data as either ID or OoD depending on the score obtained. When studying how OoD samples emerge, it's important to distinguish between two fundamentally different scenarios: *semantic shifts*, which occur when samples that do not belong to any class start to emerge, changing the overall distribution of the input space without truly altering the distribution of the previously seen classes; and *covariate shifts*, which occur when the inherent distribution of one or several classes shifts from its original distribution. In this context, OoD detection only covers the detection of semantic shifts in the data, as covariate shifts are covered by the branch of anomaly detection [20]. Based on the review from Yang et al. [1], OoD detection algorithms can be categorized into four distinct heuristics based on the information used to detect OoD samples: classification-based, distance-based, density-based, and reconstruction-based methods. Our paper focuses on distance-based techniques, which rely on the distances within the latent space to define the desired OoD scoring function. Due to the lack of literature on OoD detection in networks trained using the FFA, we will provide a comparative perspective on methods employing backpropagation BP.

Currently, the ODIN algorithm stands as the most widely-used benchmark for OoD detection due to its high accuracy and reduced computational costs. This algorithm operates by measuring the effect on the softmax distribution of the last layer when changing the temperature scaling and introducing small perturbations into the inputs, where OoD samples result in the greatest differences [21]. An alternative approach was proposed by Bergman et al., where the deep k-nearest neighbor algorithm is employed to measure the distance between input samples and previously computed ID representative latent manifolds, thereby using the latent distance to detect anomalies [22]. Building upon this research, Sun et al. extended the application of the deep k-nearest-neighbor distance for OoD detection [23], highlighting the importance of exploiting the geometric properties in the latent space of trained networks for OoD detection tasks. Despite the extensive literature on this task, a noticeable gap exists in the context of techniques designed specifically for spiking neural networks. In their recent work, Martinez-Seras et al. introduced a novel method for OoD detection that focuses on spike count patterns in the latent space. By characterizing spike patterns across various layers, they identify whether a given spike pattern aligns with those extracted from in-distribution data [24].

2.4 Explainability and Interpretability

Explainable AI, commonly referred to as *XAI*, is a field focused on developing techniques to offer humanly understandable explanations for the motivations behind a model’s outputs. It is well acknowledged that most modern models operate as black boxes, achieving high performance across multiple tasks but offering little to no insight into the heuristics they follow to obtain their outputs. To address this shortcoming, the *XAI* field encompasses multiple subtopics aimed at extracting different types of knowledge of models. Among these subtopics, the most relevant are given by: understandability, comprehensibility, interpretability, explainability, and transparency. This paper focuses on *Interpretability*, which aims to extract meaningful explanations that can be easily understood by humans agents.

As of now, the most prevalent interpretability techniques for computer vision tasks are driven by Class Activation Maps (CAMs) [25], which create visual insights highlighting the most significant regions of an input image that impacted the prediction. Among methods providing this type of explanation, *Grad-CAM* stands as the one with the greatest impact. This method uses the gradient information of the last convolutional layer to detect the areas of the input that had the highest impact on the prediction of a specific class [26]. Although several extensions of the algorithm have been developed to enhance the quality of the attribution maps [27, 28], these methods are not applicable to spiking networks due to their reliance on precise gradient information, which cannot be obtained from spiking networks because of the non-differentiability of their neural model. To overcome this issue, Kim et al. introduced a visualization algorithm named Spike Activity Mapping, which leverages the temporal dynamics of SNNs to compute neuronal contribution scores during forward propagation based on the history of spikes [29]. Another approach proposed by Bitar et al. addresses the gradient issue in image attribution by employing surrogate gradients, demonstrating their capability to maintain sufficient accuracy for effectively modeling the saliency map [30].

Contrasting with these approach, which rely solely on gradient information, Martinez et al. presented a technique involving a backward pass of a latent vector through the network to compute the relevance of specific features in the input space [24]. This method operates by reconstructing spike patterns across the layer and enabling the quantification of feature activity, thereby identifying regions of significance within the image. By doing so, the authors place additional focus on exploiting the representational capabilities of the latent space of non-convolutional networks to create interpretable techniques. Our paper follows the same geometrical motivation, leveraging the specific latent topology of FFA to provide enhanced interpretable results.

2.5 Contributions

This work presents a seamless adaptation of FFA for spiking models, offering an alternative formulation to the one proposed by Ororbia in [6]. In our formulation, we introduce two alternative goodness functions: an unbounded goodness function, which follows Ororbia’s methodology by treating spikes as a discrete version of ReLU activation; and a bounded goodness function, which fully leverages the bounded behavior of spiking models, making it more suitable for neuromorphic computers. Subsequently, we develop FF-SCP, an OoD detection algorithm that capitalizes on the characteristic latent space observed by the community to enhance the robustness of FFA. The applicability of FFA’s geometrical properties remains impactful for creating software that meets industry requirements in terms of security. However, the current trend in the literature has primarily focused on its predictive capabilities. Thus, this work offers an initial step toward providing additional methodologies that bring FFA closer to being a robust alternative to BP in terms of functionality. Additionally, to further explore the functional aspects of the latent space of FFA, we develop an attribution algorithm that provides understandable explanations for the features of an image that push it outside the distribution of any given class. This work also contributes to expanding the literature advocating for the study of the geometrical properties of latent spaces to benefit model reliability, particularly from the explainability field. However, we acknowledge the intrinsic challenge posed by the lack of better-suited architectures when introducing FFA into production-ready software.

3 Proposed Approach

This section introduces the methodological aspects of the algorithms proposed in this work, dedicating one subsection to each of the contributions. Subsection 3.1 outlines the adaptation of FFA for SNNs. Subsection 3.2 introduces the FF-SCP algorithm, which employs the latent state of SNNs trained with FFA to create an OoD detection algorithm. Lastly, Subsection 3.3 presents an attribution technique aimed at providing visual insights into the information relating arbitrary samples to the distribution of specific classes.

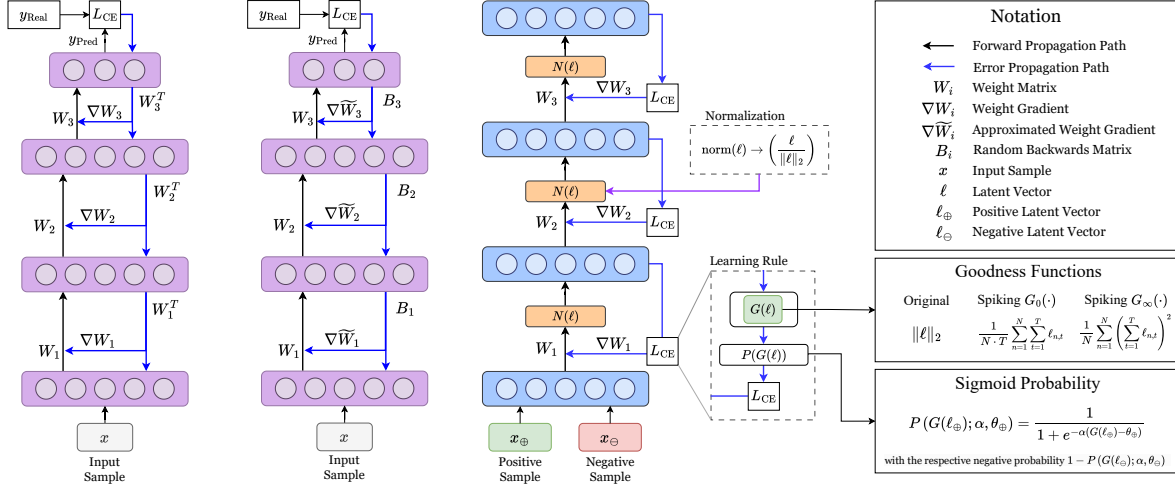


Figure 1: Diagram illustrating the architecture, from left to right, of Backpropagation (BP), Feedback Alignment [31], and Forward-Forward Algorithm (FFA) [3]. Each architecture highlights the input forward path (black arrows), and the error propagation path (blue arrows). Additionally, we describe the update mechanism of FFA and its spiking adaptations.

3.1 Spiking Forward-Forward Algorithm

Although the original motivation that led to the development of FFA was to propose a biologically plausible alternative to BP, the vast majority of research on this method is still obtained using ANNs. In this section, we present a straightforward adaptation of FFA for SNNs, modifying the goodness scoring function to aggregate the temporal dimension and employing surrogate gradient techniques to enable training under standard ML pipelines. Additionally, to capitalize on the bounded dynamics offered by spiking models, we propose a novel bounded goodness function that operates independently of the total simulation time. For the remainder of this paper, we will denote the spiking formulation of FFA as *sFFA*.

As detailed in Section 2, the original goodness function G was formulated using the squared Euclidean distance of the latent vector. This function, combined with the unbounded dynamics of ReLU activations, enabled learning dynamics that could result in positive latent vectors achieving arbitrarily high goodness scores as training progressed. However, due to the discrete event-driven nature of SNNs, where the latent space consists of binary latent vectors, the activation value of each neuron is bounded by the total number of timesteps in the simulation. Therefore, to replicate behaviors similar to those observed in ANNs, the goodness function must be adapted to handle these discrete binary states. This paper introduces two implementations of the goodness function for spiking models: an *unbounded goodness*, which mimics the behavior of ANNs through the aggregation of the temporal dimension; and a *bounded goodness*, designed to capitalize on the bounded activation range of SNNs.

The first goodness function, namely the unbounded goodness function, referred to as $G_{\infty}(\cdot)$, can be naturally adapted from the conventional goodness function by considering the sum of spikes as a linear approximation of ReLU-like functions. In this scenario, the goodness function takes the latent vector ℓ , composed of the spike train of the neurons of the layer, and acts as the squared Euclidean norm of the number of spikes. Formally, given the latent vector $\ell \in \{0, 1\}^{N \times T}$ consisting of N neurons and T timesteps, the function $G_{\infty}(\ell) : \{0, 1\}^{N \times T} \rightarrow \mathbb{R}_{\geq 0}$ is formulated as:

$$G_{\infty}(\ell) = \frac{1}{N} \sum_{n=1}^N \left(\sum_{t=1}^T \ell_{n,t} \right)^2, \quad (4)$$

where $\ell_{n,t}$ denotes the value of the n -th neuron at timestep t .

Our second goodness function, namely the *bounded goodness*, denoted by $G_0(\cdot)$, offers an alternative formulation in which the learning process relies solely on bounded states, aligning more closely with biological models compared to their unbounded counterparts. To achieve this, we replace the squared Euclidean distance with the Manhattan distance of the mean number of spikes in the latent spike train, ensuring all neurons contribute equally to the goodness score. Moreover, by applying mean aggregation, the obtained goodness scores remain independent of the total number of timesteps. Formally, given the latent vector $\ell \in \{0, 1\}^{N \times T}$, the *bounded goodness* function $G_0(\ell) : \{0, 1\}^{N \times T} \rightarrow \mathbb{R}_{\geq 0}$

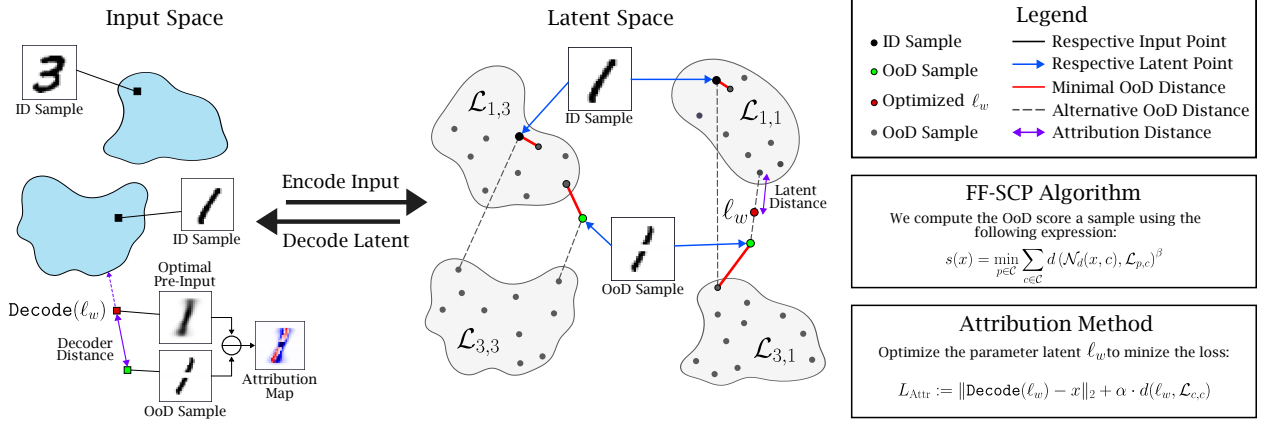


Figure 2: Visual diagram providing an example of the mechanics of our FF-SCP algorithm on an OoD sample using the latent space of classes 1 and 3. Additionally, we depict our interpretability method to obtain the attribution map of the OoD sample against the latent manifold of the class 1.

is expressed as:

$$G_0(\ell) = \frac{1}{N \cdot T} \sum_{n=1}^N \sum_{t=1}^T \ell_{n,t}. \quad (5)$$

Upon early inspection of both goodness functions, several properties can be noted. On one hand, the unbounded function $G_\infty(x)$ is not strictly unbounded, as it spans an interval defined by the number of neurons N and the total timesteps T , $[0, N \cdot T^2]$. However, the upper limit of this interval can achieve sufficiently high values to approximate the behavior of unbounded models. Moreover, this upper limit can be easily adjusted by changing the values of these two parameters, allowing for higher scores to approximate the behavior of unbounded models. On the other hand, the bounded design of $G_0(x)$ results in a range confined to the interval $[0, 1]$, regardless of the aforementioned parameters. This bounded limit can pose challenges in achieving extreme values of the probability function $P(\cdot)$, especially if the original threshold θ was intended for unbounded goodness scores, as the function’s range will not properly span the probability range $[0, 1]$. To address this, we modify the probability function in two ways. First, we introduce a scalar factor α to scale the term $G(\ell) - \theta$. Second, we replace the single threshold θ with two thresholds, θ_\oplus and θ_\ominus , applying independent thresholds to the positive and negative probability functions, respectively. This adjustment allows us to increase α and adjust $\theta_\oplus, \theta_\ominus$ to align with the domain of the probability function. Under this formulation, the resulting probability function is expressed as follows:

$$P(G(\ell_\oplus); \alpha, \theta_\oplus) = \frac{1}{1 + e^{-\alpha(G(\ell_\oplus) - \theta_\oplus)}}, \quad (6)$$

where the converse negative probability function is defined by the expression $1 - P(G(\ell_\ominus); \alpha, \theta_\ominus)$.

3.2 The FF-SCP Algorithm

This section introduces the FF-SCP algorithm, which leverages the emergent representational properties in the latent space of FFA to detect OoD inputs. As previously mentioned, multiple studies have observed that the latent space of networks trained using FFA exhibits a distinctive topology, characterized by distinct clusters for each training class [5, 4]. Conversely, due to ReLU activations having a minimum value of 0, negative data tends to generate near-zero latent vectors, resulting in all negative data clustering around the origin of the latent space. However, due to the inherent noise present in spiking models, negative latents attain higher activity bounds, shifting the single cluster of negative data into multiple different clusters dispersed throughout the space. These clusters retain the representability of the space, as each one can be observed to contain samples from the same class and which employed the same embedding label. Despite the presence of a high number of clusters, the neural specialization of the neurons contributes to creating a highly separated latent space, which is a desirable property for detecting samples not drawn from the training distribution. A visual representation of the emergent latent spaces is provided in Appendix B.

In its original formulation, the SCP algorithm proposed using a class-representative latent vector to describe each class, so that the geometric complexity of the latent space could be reduced into a single characteristic vector. To achieve this, SCP employed the centroid of the class latent vectors, allowing for straightforward computation of the

OoD score by measuring the distance between the centroids and the sample’s latent vector representation. However, this representative vector failed to perform adequately when presented with data distributions whose latent subspaces resulted in separated topologies or highly unbalanced latent vector distributions, as the center of the data did not capture the complex geometry of these latent manifolds.

To mitigate this effect, this work proposes an alternative distance heuristic, replacing the centroid distance with a point-set distance between the latent vector $\ell \in \mathbb{R}^N$ of a sample x and a set of latent vectors $\mathcal{L}_c = \{\ell^1, \ell^2, \dots\}$ extracted from the complete latent manifold of class c , where N is the dimension of the layer. This distance function is formulated using a prior distance function $d(z_1, z_2)$, which measures the distance between two arbitrary vectors $z_1, z_2 \in \mathbb{R}^n$. The distance between a point and a set is then defined as the minimum distance between the point and any point in the set. From a theoretical perspective, this function should operate over the complete latent manifold $\overline{\mathcal{L}_c} \subset \mathbb{R}^N$, however, due to the discrete nature of current AI, these clusters can only consist of a finitely many set of points. Therefore, we approximate this distance using the following expression:

$$d(\ell, \overline{\mathcal{L}_c}) = \inf_{\ell \in \overline{\mathcal{L}_c}} d(\ell, \ell) \approx \min_{\ell \in \mathcal{L}_c} d(\ell, \ell). \tag{7}$$

Given that FFA provides different representations of the same input sample x depending on the embedded label p used during the supervised inference process, the input data used to create the latent space representatives must include both positive and negative instances of input data. Therefore, creating the set \mathcal{L} of the different clusters must involve a uniform amount of inputs from each class using all possible labels and storing them. Once all these vectors have been captured, the set \mathcal{L} will provide a sufficient representation of the original latent space.¹ To account for the presence of negative vectors, we extend the definition of \mathcal{L} to $\{\mathcal{L}_{c,p} \mid c \in \mathcal{C} \text{ and } p \in \mathcal{C}\}$, where $\mathcal{L}_{c,p}$ represents the set of latent vectors from class c forwarded using the embedded label p , and \mathcal{C} denotes the set of class labels.

Once the representative set of latent vectors has been identified, an initial version of the scoring function can be formulated as the distance between the sample’s latent vector and each class-representative set of clusters. Unlike conventional neural networks, where the latent representation of a sample is unique, FFA generates different representations depending on the embedded label used during the forward process. Therefore, to measure the distance between a sample and the set of class-representative clusters, it’s crucial to account for the different representations that the sample obtains with different labels. Thus, the distance from the latent vector to each class is defined as the sum of the distances from the vector to each of the class clusters. This effect is illustrated in Figure 2, where the red lines define the distances from each latent vector of the different embeddable labels with respect to the latent representative sets $\mathcal{L}_{c,p}$.

Consequently, the score of the unknown sample x is defined as the minimum distance from its latent representation to each class representative set of clusters. Once this minimal distance is computed, ID samples are expected to achieve a low overall distance, as their representation should remain proximal to their respective class set of clusters. Conversely, OoD samples are expected to attain a higher minimal distance, as their latent vectors should not be within proximity to any set of ID clusters. Therefore, the initial score function can be defined as:

$$s(x) = \min_{p \in \mathcal{C}} \sum_{c \in \mathcal{C}} d(\mathcal{N}_d(x, c), \mathcal{L}_{p,c})^\beta, \tag{8}$$

where $\mathcal{N}_d(x, p)$ represents the output latent vector obtained from the forward pass of an input x with the embedded label p at depth d , and β denotes a scaling hyperparameter.

When working with certain spaces, this scoring function can encounter a significant limitation, as an insufficient number of samples can result in inaccuracies when measuring the discrete approximation of the distance. For instance, in scenarios where the latent representation contains widely dispersed points, the resulting measurements will tend to lean towards large distances, as the distance approximation might fail to find nearby neighbors. This issue is more pronounced in high-dimensional spaces, where the curse of dimensionality requires exponentially more samples to achieve even distributions of points as the dimensions increase. Furthermore, due to the activity maximization objective of FFA, where positive latent vectors strive to maximize their distance from the origin, class manifolds can see their diameters extended over large distances, making it harder to achieve accurate representations.

In such scenarios, an extreme outcome can occur where the scoring of samples is inverted, leading to OoD samples achieving lower scores than ID samples. This situation arises when the minimal distance from the zero vector to any

¹Given that networks trained with FFA do not currently achieve state-of-the-art accuracy, a filtering step is necessary to remove potentially misclassified latent vectors. This step involves discarding a small set of the least active elements from sets where the embedded label aligns with the real class, as they may have been misidentified as negative samples. Conversely, it also involves removing a reduced set of the latent vectors with the highest activity from the negative sample set to avoid potential misclassification of these highly active elements as positive samples.

representative cluster is smaller than the distance between points within the same representative cluster. Consequently, OoD samples, typically characterized by nearly zero latent activity, can end up with lower scores than ID samples with high latent activity, simply because they are unable to find a nearby neighbor within their own cluster to minimize the scoring function. Formally, this issue arises when the following inequality holds:

$$\min_{c \in \mathcal{C}} d(\mathbf{0}, L_{c,c}) \leq \mathbb{E} \left[\min_{c \in \mathcal{C}} d(\mathcal{N}_p(\mathbf{X}, c), \mathcal{L}_{c,c}) \right], \quad (9)$$

where \mathbf{X} represents a randomly selected sample in the ID dataset. A more detailed explanation of this result is presented in Appendix A.

To mitigate this issue, an additional branch is incorporated into the function, so that the samples satisfying this condition are handled separately. Within this branch, instances closer to the zero vector than to any other class cluster are assigned a large value γ . This designation indicates that these instances are more likely to belong to the negative distribution, which consists of synthetic samples outside the training distribution. However, we acknowledge that a small proportion of ID samples may also fall into this category. For these instances, a greater distance from the zero vector suggests a higher likelihood of misclassification. Therefore, we introduce a negative $s(x)$ term into the expression so that elements that fall into this branch have their order reversed.

Therefore, after the proposed changes, the final scoring function is given by:

$$S(x) = \begin{cases} \gamma - s(x), & \text{if } s(x) > z_s \cdot s_0(x) \\ s(x), & \text{otherwise,} \end{cases} \quad (10)$$

where γ denotes a constant value designed to assign an elevated score to samples falling into the first branch, the term $s_0(x)$ represents is equivalent to the function $s(\cdot)$ but replacing the spaces $\mathcal{L}_{i,j}$ for the space comprised by the vector $\mathbf{0}$, and z_s serves as a scaling factor for the zero distance s_0 .

Once the scores of the data are computed, the labeling of OoD samples follows a conventional process. This is achieved by comparing the score obtained by a sample with a manually chosen threshold value. If the score of the sample is greater than the threshold value, the sample is classified as OoD; conversely, if the score is less than the threshold, the sample is identified as ID. The threshold value is user-defined, depending on the desired confidence level for the model to operate. Therefore, the final heuristic used with FF-SCP is detailed in Algorithm 1.

3.3 Interpretation of Latent Vector

Our FF-SCP algorithm presents a method to provide robustness guarantees for AI products. However, this OoD detection method only offers a quantitative measurement indicating the extent to which a sample does not belong to the training dataset. To enhance the functionality of this algorithm, this section introduces a novel interpretability algorithm designed to produce human-understandable explanations of the decisions made by FF-SCP. Given an input sample x , this algorithm generates an attribution map highlighting the features that do not align with those expected from the data distribution of a selected class c . This method leverages the same latent space approximation used by FF-SCP, employing a large sample set of latent vectors to approximate the emerging topology from the network’s activity (see `initialize_latents` in Algorithm 1). By exploring this latent space, our algorithm identifies the closest neighbor x_f of the sample x , ensuring that its latent representations closely resemble those expected from the latent data of class c while retaining key features that characterize the original input x . A visual representation of this process is illustrated in Figure 2.

To search the latent space for the desired ID sample x_f , we employ a decoder network that accurately maps the latent space back to its pre-image space in D_{\oplus} . Networks trained using FFA are known to provide accurate projections of the input images, capturing the key distinctive features of this input space, thus allowing for precise reconstruction of the latents [5]. Consequently, we can assert that latent vectors surrounding the latent class manifold will result in plausible reconstructions, not distant from those present in the training dataset. We denote the application of this decoder network as `Decode` : $\mathbb{L} \rightarrow D_{\oplus}$, which is trained using the input-latent pairs from the positive dataset. It’s important to note that while negative samples belong to the latent space of the network and provide accurate representation probabilities, they do not align with the features expected for the ID data. Therefore, to obtain the features that cause an input sample to deviate from the ID of a specific class, it is important to create a decoder that operates exclusively within the positive distribution.

Our algorithm operates by employing this decoder network to explore the obtained latent space approximation to find an alternative sample x_f , derived from the input x , so that it better fits the input distribution of a user-selected class $c \in \mathcal{C}$. This exploration is achieved by using a parameter latent vector ℓ_w , whose reconstruction results in our desired input vector x_f . This vector is optimized using a gradient descent algorithm to minimize two key distances: first, the

Algorithm 1: FF-SCP**Data:** Batch of input values X and their respective labels Y .**Result:** Distances to the set of averaged feature vectors

```

1 Function initialize_latents( $X, Y$ ):
  ▷ Latent Representative Generation
2   for each  $(x, y)$  in  $(X, Y)$  do
3     for each  $p$  in  $\mathcal{C}$  do
4       Obtain the latent vector  $\ell$  from  $\mathcal{N}_1(x, p)$ 
5       Append  $\ell$  into the set  $L_{y,p}$ 
  ▷ Filtering Step
6   for each  $(p, c)$  in  $\mathcal{C} \times \mathcal{C}$  do
7     if  $p$  equals  $c$  then
8       Remove the lowest normed elements of  $\mathcal{L}_{p,c}$ 
9     else
10      Remove the highest normed elements of  $\mathcal{L}_{p,c}$ 
11 Function get_score( $x$ ):
12   Define the distance vector  $\mathbf{D}$  as  $|\mathcal{C}|$  zeros
13   Define the zero distance scalar  $D^0$  to zero
14   for each  $c$  in  $\mathcal{C}$  do
15     Get the latent vector  $\ell$  from  $\mathcal{N}_1(x, c)$ 
16     Add the value  $d(\ell, \mathbf{0})$  to  $D^0$ 
17     for each  $p$  in  $\mathcal{C}$  do
18       Add  $d(\ell, \mathcal{L}_{c,p})$  to the distance to the class  $p$ ,  $D_p$ 
19   Let the score  $s$  be the minimal value in the vector  $\mathbf{D}$ 
20   return  $s$  if  $s \geq D^0$  else  $\gamma - s$ 

```

Latent Distance, which measures the displacement between the parameter latent ℓ_w and the manifold representing the latent cluster $\mathcal{L}_{c,c}$; and second, the *Decoder Distance*, which measures the distance between the pre-image x_f and the original sample x . This loss function is encapsulated in the following expression:

$$L_{\text{Att}}(\ell_w; x, \alpha, \mathcal{L}_{c,c}) = \underbrace{\|\text{Decode}(\ell_w) - x\|_2}_{\text{Decoder Distance}} + \underbrace{\alpha \cdot d(\ell_w, \mathcal{L}_{c,c})}_{\text{Latent Distance}}, \quad (11)$$

where α denotes a hyperparameter used to balance the strength of each distance. Low values of α result in latent values closer to the original image, which are desirable in cases where the overall regions do not account for a large portion of the input image. Conversely, higher values of α result in pre-images of the latent vector being closer to the input distribution of the target class, which is crucial when the distortion of the input data is large.

Once the optimization process finishes and the latent vector ℓ_w has reached an equilibrium point between the desired targets, the reconstructed sample x_f should result in the closest instance from the input space resembling the original image while belonging to the desired class. By using the difference between the original sample x and the optimal instance x_f , the obtained difference map would highlight the regions that are pushing the sample outside the desired class distribution. For instance, when an ID sample is used as the objective in this algorithm, the resulting attribution map should ideally be close to empty, indicating that the decoded latent vector closely resembles the original image with sufficient precision. However, due to the inherent noise of the decoder, some residual attribution differences may still be present. Conversely, when inputting an OoD sample with some artifacts covering the image, the attribution map obtained should highlight these artifacts with positive values, indicating that they do not belong to the ID class distribution. Meanwhile, if the OoD sample has regions of the image missing, the attribution map should highlight these regions with negative values, indicating that an image belonging to the ID distribution should have those missing parts. This final heuristic has been detailed in Algorithm 2.

Algorithm 2: Obtain Attribution Map

Data: Trained decoder on the original ID data, denoted as $\text{Decode}(\cdot)$. Objective sample data x and arbitrary class $c \in \mathcal{C}$. Latent space representative sets \mathcal{L} .

Result: Attribution map showing the differences from the sample x to the input distribution of the class c .

```

1 Function get_attribution( $x, c, \alpha$ ):
2   Initialize the parameter latent vector  $\ell_w$  to the value of  $\mathcal{N}(x, c)$ .
3   while  $\ell_w$  has not converged do
4     Compute the Decoder Distance from  $\|\text{Decode}(\ell_w) - x\|_2$ 
5     Compute the Latent Distance from  $\alpha \cdot d(\ell_w, \mathcal{L}_{c,c})$ 
6     Obtain the final loss  $L_{\text{Attr}}$  as the sum of Decoder Distance and Latent Distance
7     Update  $\ell_w$  by applying a gradient descent step on  $\nabla L_{\text{Attr}}$ ;
8   return  $x - \text{Decode}(\ell_w)$ 

```

4 Experimental Setup

To systematically evaluate the methods presented in this work, we outline 3 Research Questions (RQs) that encapsulate the conditions under which our initial hypothesis would be satisfied, thereby establishing the practical utility of FFA. The chosen research questions are:

1. **RQ1:** Can our proposed sFFA achieve competitive accuracy compared to the original FFA?
2. **RQ2:** Does the enhanced latent representation of sFFA, utilized by our proposed FF-SCP, improve upon the baseline results of SCP and ODIN?
3. **RQ3:** Does the latent space of models trained with sFFA exhibit sufficiently representative properties to develop interpretability mechanisms?

To provide insights into the experimental process used to address these questions, we have organized this section as follows: Section 4.1 outlines the configuration employed for the different models and the training process used to address RQ1; Section 4.2 describes the experimental procedure followed to evaluate our FF-SCP algorithm in relation to RQ2; Section 4.3 presents the process used to assess the quality of the attribution maps generated by our interpretability algorithm to answer RQ3; and finally, Section 4.4 lists the datasets and data processing employed in this work. All the code for the experiments has been uploaded to https://github.com/AnonymousSquirrel1316/FFA_OOD.

4.1 Architecture and Training Process

To conduct an unbiased experimental analysis across the different network architectures, minimizing potential biases between analog and spiking networks, all models were designed to achieve equivalent behaviors. Specifically, each model consisted of two densely connected feed-forward layers, each with 1400 neurons. The analog networks employed ReLU activation functions, while the spiking networks relied on LIF neural models as a biological counterpart. To implement these spiking dynamics, we utilized the LIF class from the *snnTorch* [32] library, with the following hyperparameters: a *fast sigmoid* as the surrogate function, 20 timesteps per forward pass; a threshold of 0.4 for the first layer and 0.3 for the subsequent layer; and β_n values of 0.4 for the first layer and 0.2 for the subsequent layer. To prevent spiking neurons from entering over-excited states, an input downscaling technique was applied. This technique involved scaling down the input to each neuron by a factor of $0.85^{N_{\text{Spikes}}}$ at each timestep, where N_{Spikes} denotes the total number of output spikes from the respective neuron. This approach effectively reduces the input activities of highly active neurons over time, thereby moderating their overall activity throughout the timesteps.

The training process for all models followed the supervised methodology proposed by Hinton [3], wherein positive and negative samples are generated by embedding an encoded version of the label into the image. In addition to Hinton’s proposed negative generation process, we also employed a greedy negative generation method. In this approach, the negative label is chosen as the one which maximizes the goodness score, aiming at increasing the distance between the goodness scores of positive and negative labels. Each method was independently used to train each network, and the one resulting in higher accuracy was selected for further experimentation to ensure optimal predictive capabilities for subsequent tasks, including OoD detection and our attribution method. Additionally, we adopted the label initialization and embedding techniques proposed by Lee et al. [17], where embedding vectors of class labels are set as random binary vectors appended at the end of the data. Each binary vector, of dimension 100, was initialized using a Bernoulli distribution with a probability of 0.1 for each element of the vector.

All networks were trained for 10 epochs with a batch size of 512, using the hyperparameterized Binary Cross Entropy loss function outlined in Subsection 3.1. The spiking networks were trained using the two goodness functions developed in Section 3.1: the bounded goodness, $G_0(\cdot)$, and the unbounded sFFA, $G_\infty(\cdot)$. For networks using the unbounded goodness function, the parameters were set as $\theta^+ = 6$ and $\theta^- = 2$. Networks employing the bounded goodness function used thresholds of $\theta^+ = 0.3$ and $\theta^- = 0.1$, along with $\alpha = \beta = 5$ to optimize the scaling of the probability function. We employed the ADAM optimizer with a learning rate of 0.001 for ANNs and 0.002 for SNNs. These values were determined through a process of early experimentation and manual tuning.

4.2 Out-of-Distribution Evaluation Setup

As this paper builds upon the groundwork of the original SCP algorithm introduced in [24], and given the absence of subsequent spiking-specific OoD detection methods in the literature, the benchmarks used for this work are extracted from the aforementioned study. Specifically, the SCP and ODIN algorithms stand as the top-performing approaches, serving as the designated benchmarks for comparative analysis in this work. Furthermore, to demonstrate the competitiveness of our algorithm in the spiking domain compared to its analog counterpart, both types of networks have been tested.

The models used in these experiments are the best-performing ones from the training experiments of RQ1. We explored the use of Euclidean, Manhattan, and Cosine distances for the distance function $d(\cdot, \cdot)$, and chose the Manhattan distance due to its superior performance. We employed 1024 samples to create the latent space, following the process detailed in the `initialize_latents` function of Algorithm 1. For the filtering step, we removed 20% of the highest and lowest latent vectors from their respective latent sets. The hyperparameters γ , β , and z_0 were selected through an early hyperparameter selection process for each training and goodness. Their search space was defined as follows: z_0 was chosen from the set $\{0.85, 1, 1.15, 1.4\}$; γ was either 10^4 or 10^6 ; and β was set to either 1 or 2, representing Manhattan or Euclidean aggregation of distances, respectively.

To objectively evaluate the model’s OoD detection performance across the experiments, three key evaluation metrics have been measured: AUROC, AUPR, and FPR95. These metrics are widely employed in the OoD detection literature, providing valuable insights into the model’s ability to distinguish between in-distribution and out-of-distribution samples. Their definitions are as follows:

- *AUROC*, also known as the Area Under the Receiver Operating Characteristic Curve, is a threshold-independent metric that, when given a set of OoD scores for the data, quantifies the extent of overlap between OoD and ID samples. The AUROC metric ranges from 0 to 1, where 0.5 indicates a random classifier’s performance, and 1 signifies a perfect classifier that can perfectly separate OoD and ID samples.
- *AUPR*, also known as the Area Under the Precision-Recall Curve, considers the precision and recall trade-off in classifying OoD samples. AUPR values closer to 1 indicate better performance, with high precision and recall in distinguishing OoD samples.
- *FPR95*, also known as the False Positive Rate at a 95% True Positive Rate, provides insights into the model’s false positive rate when the true positive rate is set at 95%. This metric quantifies the model’s ability to maintain a low false positive rate while correctly identifying 95% of OoD samples. Lower FPR95 values are indicative of better OoD detection performance.

4.3 Evaluation of the Quality of the Attribution Method

As mentioned in Section 3.3, our proposed interpretability algorithm provides a visual representation of the areas that drive images towards the OoD direction. Given the subjective nature of evaluating the quality of an attribution map, we rely on a qualitative analysis of several samples from the training data. We conducted this analysis using instances from the MNIST and KMNIST datasets, generating altered images through several obstruction methods to measure our method’s performance when presented with closely resembling images. The artifacts introduced in these images serve as primary factors pushing them towards the OoD direction, and thus, should be the most prominent regions highlighted on the attribution maps. The samples chosen for evaluation were randomly selected from both datasets, and after comprehensive inspection, those that most clearly embody the characteristics captured by the attribution map were retained for further analysis. This analysis focuses on identifying the attribution capabilities of the approach and uncovering potential limitations.

The decoder network chosen to reconstruct the latent spaces is a single-layer analog network utilizing Sigmoid activations. To prepare the spike train vectors for the analog decoder, these latent vectors are averaged over the time dimension. During training, the decoder minimizes Binary Cross Entropy loss between the input image and the reconstructed image generated from the latent vector obtained from the first layer. This loss function was preferred due

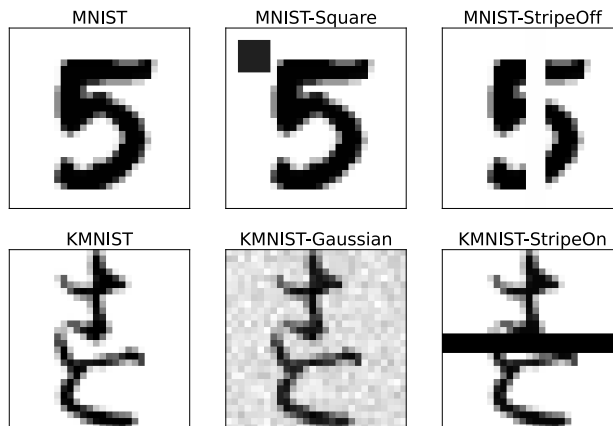


Figure 3: MNIST and KMNIST dataset samples with applied obstructions for attribution experiments. Each row begins with an in-distribution sample from the respective dataset, followed by its obstructed versions.

to its ability to produce more accurate results compared to regression-based losses. Similarly, we chose to extract latent vectors from the first layer because of its accurate reconstructions. The decoder was trained for 50 epochs using the ADAM optimizer with a batch size of 512 and an initial learning rate of 0.001. Additionally, an exponential decay on the learning rate was applied, with a gamma decay of 0.4 every 5 epochs. The value of α has been manually tuned in each experiment, and the one resulting in the best attribution map has been selected.

The obstruction techniques employed in these experiments include: *Square*, which introduces a 5×5 square at a random corner of the image, positioned 2 pixels away from the borders of one of the corners; *Gaussian*, which injects random Gaussian noise into the image, drawn from the normal distribution $\mathcal{N}(0, 0.2)$; *StripeOff*, which eliminates a random vertical or horizontal stripe of 3 pixels from the image, with the removal occurring within the center (pixels from 12th to 18th row or column); and *StripeOn*, which adds a random vertical or horizontal stripe of 3 pixels to the image within the center (pixels from 12th to 18th row or column). All proposed obstruction methods are illustrated in Figure 3.

4.4 In-Distribution and Out-of-Distribution Datasets

To evaluate the training accuracy of our adaptation of FFA to spiking networks, we employed five well-known datasets: MNIST [33], consisting on 60,000 images of 10 classes of handwritten digits; Fashion MNIST [34], composed of 60,000 images representing 10 classes of clothing items; Kuzushiji-MNIST (KMNIST) [35], consisting of 60,000 images of Japanese characters divided into 10 different classes; and EMNIST (Letters) [36], composed of 145,000 images of the 26 lowercase letters of the Latin alphabet. A uniform normalization pipeline was applied across all datasets. Each of these spike trains was set to last for 20 timesteps.

Since OoD experiments require a trained model and its corresponding training dataset as the ID baseline, we utilize all the models previously trained in RQ1 for experimentation in RQ2. In these experiments, the OoD dataset is constructed by combining all other training datasets on which the models were not trained. To expand the scope of our analysis, we introduce two additional OoD datasets: Not-MNIST (small) [37], which consists of 19,000 font glyphs representing letters A to J, and Omniglot [38], containing 1,623 handwritten images spanning 50 different alphabets. These datasets underwent the same data processing pipeline used in the training experiments.

4.5 Limitations

This work proposes FFA as a candidate alternative to BP, highlighting its functional latent space and representational capabilities, which offer substantial advantages for developing techniques to enhance model robustness for industry-ready software. However, due to the early stage of research into this algorithm, we observed a clear lack of alternative architectural formulations (e.g., convolutional or transformer layers). To date, only one work has presented a possible design for a convolutional layer in FFA by relying on pattern-like embeddable patterns [39]. While this method demonstrates accurate precision on small datasets, no proofs have been given of this algorithmh scaling to more complex datasets, such as CIFAR-10, where images contain non-empty backgrounds. Consequently, current models can only rely on densely connected layers, which have multiple limitations when learning from highly complex datasets. As a result of this limitation, the latent representations of these models exhibit a clear upper boundary on representational

accuracy. These inaccuracies in understanding the data can lead to suboptimal cluster distribution within the latent space, preventing effective leveraging of cluster distances for accurate OoD detection or interpretability mechanisms.

However, it is important to note that the representational properties of FFA arise from its learning dynamics, which are independent of the specific architectural choice of weights. Therefore, this paper provides an initial perspective on the practical utility of FFA in its current form, based on densely connected layers. Nonetheless, as further elaborated in Section 6, one of our primary goals for future research is to develop alternative formulations of FFA suitable for convolutional architectures, thereby extending our findings to more complex datasets.

5 Results and Discussion

This section presents the results from various experiments, discussing the findings and highlighting observed limitations. Initially, Subsection 5.1 showcases the accuracy results of our proposed spiking adaptations of FFA. Subsection 5.2 presents the outcomes of the OoD detection task using the FF-SCP algorithm, comparing it against the SCP and ODIN algorithms. Finally, Subsection 5.3 discusses the results obtained from the attribution method proposed in this paper.

5.1 RQ1: Training Results of sFFA

The accuracies obtained from the training experiments using the different goodness functions are presented in Table 1. These results demonstrate the comparable performance between the analog and the spiking implementations of FFA, where SNNs only exhibit a slight decrease in accuracy, likely due to the increased noise within latent vectors caused by the stochastic input preparation process. Among the two proposed goodness functions, the models employing the unbounded version achieved higher accuracy than their bounded counterparts, with an accuracy of 86.16% compared to 81.20%.

Nevertheless, while the average accuracy shows a noticeable drop, this loss in accuracy is primarily related to the significant difference in accuracy on the MNIST dataset, where the bounded version reduces accuracy by 14.61 points. This abnormal relationship in the drop in accuracy across different datasets suggests that the bounded and unbounded models process the data differently, leading to distinct classification heuristics and representation properties. These results align with the observation that networks using bounded goodness functions do not experimentally create sparse latent representations, which can result in reduced feature specificity in the neurons (see Appendix B).

Table 1: Accuracy of networks trained with the Forward-Forward Algorithm. The accuracies of models with a similar architecture (i.e., densely connected layers) and number of parameters have been included for comparison.

Dataset	BP Analog	FFA Analog	Spiking FFA $G_0(\cdot)$	Spiking FFA $G_\infty(\cdot)$
MNIST	98.25%	97.77%	93.27%	93.01%
FMNIST	89.47%	85.75%	83.69%	85.68%
KMNIST	92.11%	91.86%	71.30%	85.91%
EMNIST	92.19%	87.25%	76.54%	80.07%
Average	93.00%	90.65%	81.20%	86.16%

5.2 RQ2: Out-of-Distribution Detection Results

The metrics of the OoD detection experiments using our proposed method are presented in Table 2. After thoroughly analyzed the results, we conclude that they have yielded a positive outcome to our initial research question. A detailed discussion of these results follows in the present subsection.

sFF-SCP is competitive against SCP and ODIN The main hypothesis guiding the development of the FF-SCP algorithm was that the improved representation capabilities of networks trained with FFA, together with refined geometric methods, would yield higher accuracy in OoD Detection tasks. The results, as presented in Table 2, verify this hypothesis, with both the bounded and unbounded models consistently outperforming the SCP algorithm across all datasets and metrics, except for one instance. The results are particularly evident when compared against the unbounded versions of the FF-SCP, where the average AUROC is 7.95 points higher. Furthermore, the proposed algorithm exhibits a significant reduction in the FPR95, implying that it is more robust in situations where a high True Positive Rate is required. Nevertheless, the FF-SCP algorithm appears to follow the same pattern of the best and worse-performing pairs

Table 2: Results of the FF-SCP algorithm of our three proposed networks: the Analog FF-Network; the Unbounded FF-Network, denoted as $G_\infty(\cdot)$; and the Bounded FF-Network, denoted as $G_0(\cdot)$. Data from the SCP and ODIN has been extracted from the paper [24]. The ANN results are only shown as a baseline to compare ANN vs SNN.

ID Dataset	OOD Dataset	AUROC \uparrow					AUPR \uparrow					FPR95 \downarrow				
		FF-SCP Analog	FF-SCP $G_\infty(\cdot)$	FF-SCP $G_0(\cdot)$	SCP	ODIN	FF-SCP Analog	FF-SCP $G_\infty(\cdot)$	FF-SCP $G_0(\cdot)$	SCP	ODIN	FF-SCP Analog	FF-SCP $G_\infty(\cdot)$	FF-SCP $G_0(\cdot)$	SCP	ODIN
MNIST	Omniglot	91.14	90.18	89.07	71.56	94.72	94.41	92.12	91.87	71.90	94.28	37.18	29.97	34.38	88.93	29.08
	notMNIST	99.99	99.97	99.97	99.14	64.45	99.99	99.94	99.99	99.01	57.16	0.00	0.01	0.00	03.60	86.65
	FMNIST	97.97	97.87	99.37	91.21	73.97	97.87	97.71	99.40	87.15	65.29	10.54	11.72	3.34	24.95	77.11
	KMNIST	98.12	98.40	99.39	94.89	73.97	98.05	98.33	99.41	94.92	76.27	8.72	8.88	3.46	24.99	72.87
	Letters	89.63	91.60	96.85	88.11	81.43	94.62	95.72	98.45	79.49	64.19	54.62	40.12	16.00	51.66	73.89
FMNIST	MNIST	99.10	99.00	98.76	92.60	95.98	98.50	98.12	98.23	93.18	95.74	3.14	3.44	4.64	35.48	17.37
	Omniglot	98.86	98.67	96.38	84.75	97.86	98.85	98.61	97.40	85.37	97.83	3.84	4.33	15.99	63.55	09.97
	notMNIST	99.85	99.89	99.91	98.87	61.70	99.93	99.75	99.95	99.14	61.75	0.21	0.12	0.33	02.47	92.33
	KMNIST	97.44	97.82	98.05	84.56	88.36	97.20	97.16	97.82	82.41	88.84	12.84	9.13	8.97	53.10	57.39
	Letters	98.05	98.31	97.41	92.83	91.83	98.75	98.69	98.65	88.10	85.15	8.72	6.60	13.64	34.49	39.82
KMNIST	MNIST	86.26	81.93	60.73	61.85	85.79	76.83	70.23	53.89	61.64	88.57	36.11	44.11	75.78	89.34	51.64
	Omniglot	86.26	82.59	54.84	58.54	96.43	86.84	84.12	62.58	59.68	97.25	39.04	43.24	69.36	92.58	08.09
	notMNIST	95.95	91.52	99.13	96.88	67.24	98.03	88.48	99.53	96.68	67.59	28.91	18.34	3.89	09.52	81.37
	FMNIST	84.18	77.45	67.84	75.00	76.73	88.03	83.46	60.86	72.85	78.58	79.82	80.68	71.89	66.14	70.67
	Letters	73.86	79.37	82.75	78.34	85.14	79.95	82.38	84.89	64.47	80.65	59.83	48.55	44.96	71.49	53.51
Letters	MNIST	88.04	83.36	83.93	69.06	80.98	81.16	76.13	71.91	82.30	88.73	52.45	71.13	65.56	88.83	68.13
	Omniglot	81.14	82.59	84.97	77.60	97.11	78.24	78.51	77.37	88.04	98.54	63.38	54.51	45.13	87.11	15.54
	notMNIST	99.98	99.97	99.94	98.63	58.08	99.98	99.81	99.94	98.90	69.65	0.00	0.02	0.00	07.48	93.94
	FMNIST	91.62	95.94	90.78	86.33	71.30	90.13	94.56	84.58	92.08	83.66	60.02	27.63	37.70	47.30	88.04
	KMNIST	99.27	99.61	97.47	86.31	77.60	98.72	99.01	95.51	92.15	85.47	3.47	1.44	14.16	51.41	77.88
	Average	92.84	92.30	89.88	84.35	81.03	92.80	91.64	88.61	84.47	81.25	28.14	25.20	26.46	49.72	58.26
	Median	96.70	96.88	97.13	86.32	81.20	97.54	96.44	97.61	87.59	84.40	20.88	15.03	15.07	51.53	69.4

of ID and OoD datasets as the SCP algorithm, confirming the similarity between the heuristics of both methods. Both algorithms demonstrate the capability to outperform ODIN in the MNIST, FMNIST, and Letters datasets. However, they lack accuracy when used against the KMNIST dataset, where ODIN manages to outperform in several instances. A plausible explanation for the reduced results on the KMNIST as an ID dataset may arise from the suboptimal test performance exhibited by networks using FFA. Upon examining the weights they generate, they demonstrate less specificity, allowing for easier OoD samples to exhibit similar latent vectors to ID samples. Additionally, consistent with the findings of Martinez-Seras et al., the Omniglot dataset remains the poorest performing as an OoD dataset, with ODIN outperforming both algorithms [24].

Bounded vs Unbounded Goodness in FF-SCP Both goodness functions show remarkable similarity across most tasks in the benchmark, with the highest accuracy alternating depending on the specific task. However, the bounded goodness displays suboptimal accuracy in the KMNIST task, with numerous outcomes falling below 70 in terms of AUROC. This performance discrepancy may be attributed to the fact that the latent vectors of the bounded network lack sparsity, resulting in less specialization within the representation. This lack of neural specialization, together with the non-competitive accuracy on the dataset, may be explained by class clusters not achieving enough distance between them, thereby explaining the low accuracy when using the FF-SCP algorithm.

SNNs compete with ANNs when employing FF-SCP To ensure that SNNs offer practical advantages over ANNs, it’s essential to verify that their performance is not significantly overshadowed by their analog counterparts. Such a scenario would suggest that the architectural benefits of SNNs, such as inference speed and energy efficiency, might become secondary to accuracy advantages. The results presented in Table 2 demonstrate how the FF-SCP employed with unbounded goodness on SNNs yields outcomes comparable to its analog counterpart. Both methods achieve AUROC accuracies with an average difference of less than one point. Analog networks using FF-SCP perform slightly better than SNNs in average AUROC and both average and median AUPR. Conversely, both SNN goodness functions achieve superior results in median AUROC and both FPR95 measures. Examining specific instances, the worst result in analog networks is approximately 5 points below the worst result in its unbounded spiking counterpart. The bounded SNN counterpart experiences an additional drop when presented with KMNIST as the ID dataset, primarily due to the previously mentioned lack of test accuracy. However, the overall difference in accuracy is minimal, with this bounded version achieving higher AUROC in multiple cases. Nevertheless, the discrepancies between both spiking algorithms are minimal, suggesting that they offer similar results.

Importance of the scoring $S(x)$ over $s(x)$ As detailed in Subsection 3.2, the FF-SCP algorithm requires an additional conditional branch to ensure that the ordering in the scoring function is not reversed when the condition specified in Equation (13) is satisfied. To empirically demonstrate the necessity of this modification, the results obtained on the same benchmarks using the FF-SCP algorithm with the scoring function $s(x)$ are presented in Table 3, in Appendix C.

In these results, the impact of this modification becomes evident when the ID dataset is KMNIST and the OoD dataset is FMNIST, where the AUROC drops significantly to 32.95 under models trained with the unbounded sFFA and to 17.92 for analog networks. However, when the condition specified in Equation (13) does not hold, the algorithm remains capable of accurately detecting OoD samples. This is particularly observed in the bounded version of the goodness, where the latent space exhibits highly active latent vectors, consistently avoiding the reversal in the scoring values.

Statistical significance The obtained accuracy results across distinct models exhibit high similarity, posing a challenge in establishing clear evidence of the statistical significance of their outcomes. To address this, we rely on two widely used statistical methods. First, a Critical Difference Diagram [40], which incorporates a post-hoc Nemenyi test to calculate the critical distance value. This diagram orders various techniques based on their average rank, helping visualize the differences. If the average rankings of two methods are separated by less than the critical difference value, they are considered statistically equal; otherwise, they are considered statistically different.

Secondly, Bayesian posterior analysis measures the paired performance scores obtained from two different techniques. In their work [41], Benavoli et al. use a Monte Carlo sampling technique to estimate the likelihood of one technique outperforming another. This analysis distinguishes three outcomes: two indicating algorithmic superiority and one reflecting practical equivalence when the methods are statistically indistinguishable. The practical equivalence is adjusted by a hyperparameter called *rope*, which establishes the minimum difference between technique scores to consider their performance statistically different.

The first result from the Critical Distance Diagram is illustrated in Figure 4a. This diagram provides evidence of the statistical equivalence between both versions of FF-SCP and ODIN. Additionally, the analysis is consistent with the results from Table 2, showing that the representational advantages of FFA leveraged in the FF-SCP algorithm result in a statistical advantage over the SCP algorithm.

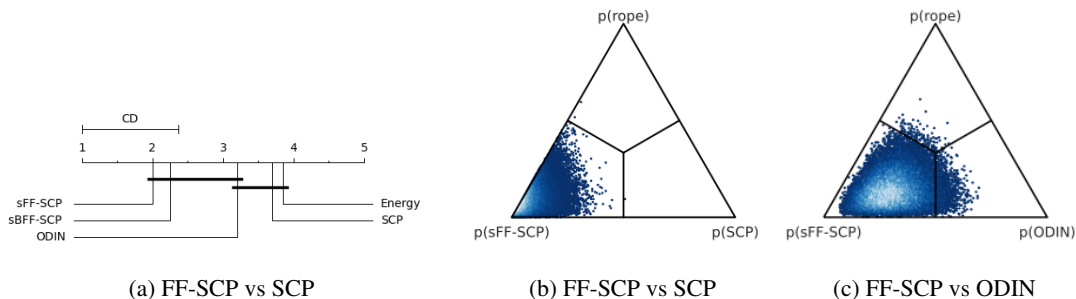


Figure 4: a) Critical Distance (CD) diagram computed over the AUROC results across the cases considered in the Tables 2 and 3. The value of CD is shown on top of the diagram. Horizontal lines connecting the average rank markers of several detectors indicate that their average rankings cannot be claimed to be different to each other with statistical significance. b) & c) Bayesian Posterior Signed Tests computed over the paired AUROC scores obtained from the FF-SCP algorithm on the Unbounded sFFA against (b) the SCP algorithm and (c) ODIN. The *rope* is set equal to AUROC = 1%. We denote by *sFF-SCP* to the application of the algorithm under the latent space of the SNN using the unbounded goodness.

The second statistical method, Bayesian Posterior Analysis, has been depicted in Figure 4b and Figure 4c. The first diagram demonstrates consistent results with the previous method, indicating that the use of FFA yields superior latent representations, resulting in improved OoD capabilities. Similarly, the results in Figure 4c reveal that the FF-SCP algorithm generally outperforms ODIN, with only a small subset of cases showing better performance for ODIN. These cases align with the observation that ODIN was able to perform better in some experiments, particularly with Omniglot as the OoD dataset and KMNIST as the ID dataset. Both algorithms exhibit almost no points within the rope region, implying that none of the methods perform equivalently, with each algorithm demonstrating statistical significance compared to the other.

5.3 RQ3: Attribution Results

To address the third research question and verify the quality of the attribution maps generated by our approach, as detailed in Algorithm 2, we have employed a qualitative analysis of several visually modified samples from the MNIST and KMNIST datasets. Recalling from the approach detailed in Section 3.3, our method provides an interpretability map

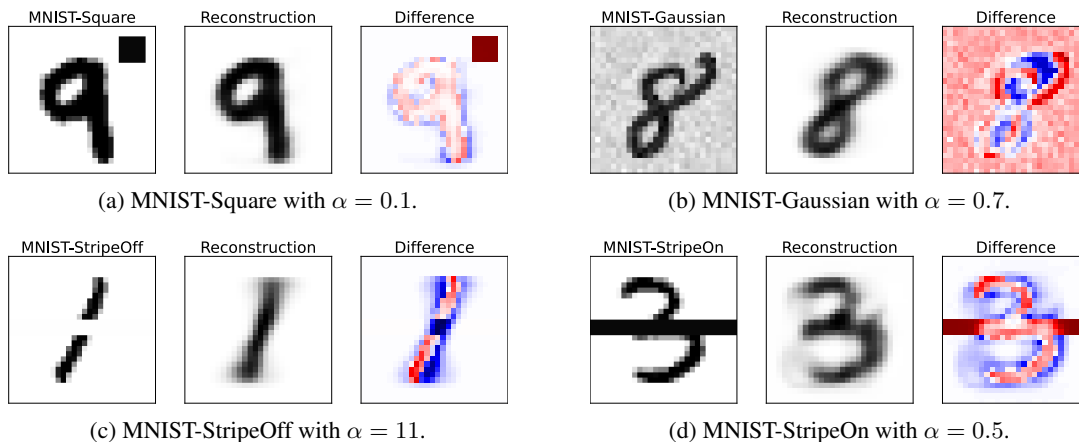


Figure 5: Batch of four visually modified samples from the MNIST dataset with their reconstructions and the corresponding attribution maps, featuring a distinct visual obstruction: (a) *Square*; (b) *Gaussian*; (c) *StripeOff*; (d) *StripeOn*.

by highlighting the regions of the image that push the original sample into the OoD space. Cold regions, represented by blue, indicate areas in the original input sample where certain features are missing compared to ID data. Conversely, hot regions, denoted by red, highlight areas in the original image that are not present in the ID data. The selected samples from the modified MNIST and KMNIST datasets are presented in Figure 5 and Figure 6 respectively.

One initial result, consistent with the findings from [5], is that the latent space provides sufficient representation capabilities to offer accurate reconstructions without excessively losing the overall original shape. Similarly, the results of the attribution on the MNIST samples appear to provide a positive answer to RQ3, offering clear attribution maps that directly highlight the incorporated artifacts. For instance, the clearest example can be observed in Figure 5a, where the included square is clearly depicted as an artifact with a high temperature, demonstrating that the primary factor pushing this sample into the OoD region is the artifact itself. A similar case is seen in Figure 5c, where the stripe is successfully localized with a cold temperature surrounding the missing area of the digit 1, showcasing the algorithm’s ability to detect instances where the figure has been split and to create a connected reconstruction. Conversely, Figure 5d has a horizontal stripe embedded into the image, which the algorithm detects and erases, preserving the prior regions of the number that overlap with the stripe. The final selected example is Figure 5b, where the algorithm demonstrates its ability to reduce noise while preserving the shape of the digit. However, a noticeable change in the upper part of the number is apparent, which may arise due to the uncommon trace compared to the most representative samples of the class, which tend to have a closed loop instead of the open end.

Among the selected examples, the attribution map that best highlights the artifact is present in Figure 5a. This additional precision, compared to the other samples, can be attributed to the lack of overlap between the original digit and the artifacts, allowing the algorithm to solely highlight the altered regions. In contrast, all other samples present slight alterations along the border of the digits, which do not appear to affect the topology of the digit. However, the degree of this deformation is not significant enough for a human evaluator to misinterpret the artifacts with respect to the ID data, so the results remain easily interpretable. For instance, in its most extreme case, as observed in Figure 5d with the *StripeOn* modification, the artifact region remains the most noticeable area, easily distinguishable from the noisy contour of the number.

As pointed out in the training results (see Subsection 5.1) and further confirmed in the OoD Detection results (see Subsection 5.2), the principal weakness of FFA becomes apparent in the KMNIST dataset, where the presence of complex features from the classes hinders the network’s representation capabilities, impacting both accuracy and OoD detection results. As a consequence, a sharp drop in accuracy within the attribution maps can be observed. This becomes evident when comparing results between the MNIST dataset and the KMNIST dataset, where the shape of KMNIST reconstructions is less accurate than those obtained from the MNIST dataset, resulting in noisier attribution maps. Nevertheless, the overall shape of the figure is still consistently reconstructed in most of the samples that are correctly classified.

One such instance is observed in Figure 6c, where the upper and lower limits of the character have been distorted, while the stripe artifact is properly removed and highlighted. A similar effect is present in Figure 6a, where our algorithm can properly detect the embedded square, showing the highest temperature, while the resulting character outline has been slightly modified but remains within the original class distribution. In contrast, a greater shift can be observed

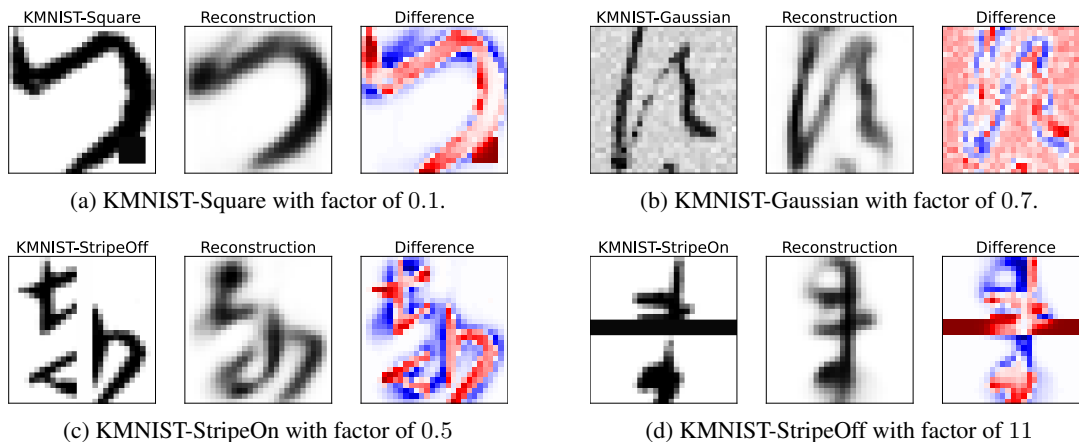


Figure 6: Batch of four visually modified samples from the KMNIST dataset with their reconstructions and the corresponding attribution maps, featuring a distinct visual obstruction: (a) *Square*; (b) *Gaussian*; (c) *StripeOff*; (d) *StripeOn*.

when the modifications to the image are more drastic. Such is the case for Figure 6d, where the obtained reconstruction is able to fill the missing stripe, but the contour appears blurred and several previously sharp features are missing, such as the upper stroke. Finally, in Figure 6b, the algorithm is able to remove a significant portion of the noise with minimal changes to the shape of the characters and only a small amount of blur. Although all samples exhibit slight perturbations and do not present clean attribution, the discriminative regions of the embedded artifacts can be clearly detected. Therefore, our results provide a positive answer to RQ3, showcasing the capability of our algorithm to create interpretable attribution maps that explain the features pushing the samples into the OoD regions. However, it is important to acknowledge the limitations that occur with suboptimal models in terms of accuracy, whose reduced representational capabilities prove detrimental to the subsequent OoD and interpretability techniques.

α Value Exploration The only hyperparameter of our method is the α value, which balances the trade-off between the distance to the class cluster and the distance to the initial image. Higher values of α bring the reconstruction closer to samples from the ID data, while lower values result in more similar reconstructions to the input images. This effect is exemplified in Figure 7, where we present several reconstructions of the sample from Figure 5c with different values of α . In the different pictures, we can observe how lower values of this hyperparameter can generate overfitted reconstructions that are not sampled from the ID cluster, keeping the digit split in two. By increasing the value of this hyperparameter, it allows for less overfitted reconstructions, connecting the two components into the corresponding number.

Since the network trained on the MNIST dataset contains accurate representations of the values, in several instances, the alpha value does not need to heavily prioritize the distance to the cluster. This effect is clear in Figure 5a, where a value of 0.1 is enough to accurately highlight the artifact in the heatmap. Conversely, there are instances where higher alpha values are required for accurate reconstructions, notably in cases where the complexity of the initial image or the artifact is higher. An example can be observed in the KMNIST dataset in Figure 6c, where, in order to properly remove the stripe from the image, higher values of alpha are required. This increase creates a sample with more distance from the original sample but increases the distance to the ID. In this case, the reconstruction is close enough to understand that the main artifact in the image is the horizontal stripe added to it.

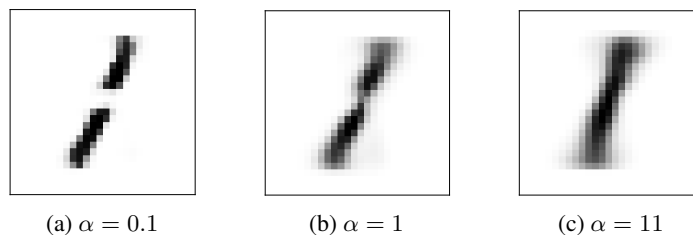


Figure 7: Reconstructions of the sample from Figure 5c with different values of α .

6 Conclusions and Future Work

The field of Artificial Intelligence has experienced rapid advancements over the last decade, even surpassing human experts in multiple tasks. However, the development of methods to ensure the robustness of these models has not kept pace with those driving performance improvements. This imbalance has resulted in the accuracy of models being overshadowed by their black-box nature when integrated into production-ready software. This issue is particularly critical in neuromorphic computing, where the temporal dynamics of spikes pose a challenge in analyzing model behavior. Nonetheless, the introduction of the Forward-Forward Algorithm (FFA) has offered a promising biologically plausible alternative learning mechanism, offering a latent space with highly representative properties. These spaces are characterized by a well-defined distribution of latent vectors that cluster with other samples from the same class while remaining distinct from instances of other classes.

This work proposes an adaptation of FFA for spiking neural networks by developing two alternative formulations of the goodness functions and utilizing surrogate gradients to circumvent the non-differentiability of the neural models. Capitalizing on the representational properties of these networks, we develop a novel Out-of-Distribution (OoD) detection algorithm, denoted as FF-SCP, which uses the distances between latent vectors and the latent manifolds of classes as an effective measure of the likelihood of a sample belonging to the training distribution. To enhance the functionality of this method, we introduce a novel attribution method that explores the latent space to generate an attribution map, highlighting features in the sample that differ from an arbitrary class. To verify the competitiveness of our FFA adaptation, we trained the network on multiple well-known datasets (e.g., KMNIST, EMNIST) and used these networks to evaluate the performance of our FF-SCP algorithm when presented with OoD samples from other conventional baselines (e.g., Omniglot, NotMNIST). Additionally, we performed a qualitative analysis on our interpretability algorithm by manually including artifacts into samples from the training data and then evaluating the quality of the generated attribution maps. Our results provide additional evidence of FFA’s capability to deliver competitive results in spiking neural networks compared to its analog formulation. Furthermore, we demonstrate how FFA can effectively detect OoD instances in spiking neural networks, outperforming SCP and ODIN. Similarly, a qualitative analysis on the distorted images shows how our method can accurately highlight the regions of the artifacts, allowing human evaluators to identify the regions pushing samples outside the image distribution. With these two algorithms, FFA proves to offer highly functional properties, resulting in a more explainable model than backpropagation.

The positive outcomes of our work pave the way for multiple future lines of research into the applicability of FFA. One clear line of research involves extending the key concepts from this work into the study of concept drift, which is critical in highly dynamic scenarios. Similarly, leveraging the findings on OoD detection by incorporating incremental learning techniques is crucial for implementing an Open-World Learning algorithm. It is also important to note that our results are limited by the lack of alternative architectures, such as convolutions or transformers, which could vastly improve accuracy in complex data domains. Consequently, one of our primary focuses will be adapting FFA to accommodate more complex dynamics, potentially enhancing performance in diverse data regimes.

Acknowledgments

This work has received funding support from the Basque Government through a number of grants: projects BEREZ-IA (KK-2023/00012) and CERBERO (KK-2024/00022) from the ELKARTEK program, a BIKAINTEK PhD grant (008-B2/2021) and the consolidated research groups Deusto for Knowledge - D4K (IT1528-22) and MATHMODE (IT1456-22).

References

- [1] Jingkang Yang, Kaiyang Zhou, Yixuan Li, and Ziwei Liu. Generalized out-of-distribution detection: A survey. *arXiv:2110.11334*, 2021.
- [2] Alec Tyson, Giancarlo Pasquini, Alison Spencer, and Cary Funk. 60% of americans would be uncomfortable with provider relying on ai in their own health care. 2023.
- [3] Geoffrey Hinton. The forward-forward algorithm: Some preliminary investigations. *arXiv:2212.13345*, 2022.
- [4] Niccolò Tosato, Lorenzo Basile, Emanuele Ballarin, Giuseppe de Alteriis, Alberto Cazzaniga, and Alessio Ansuini. Emergent representations in networks trained with the forward-forward algorithm. *arXiv:2305.18353*, 2023.
- [5] Alexander Ororbia and Ankur Mali. The predictive forward-forward algorithm. *arXiv:2301.01452*, 2023.

- [6] Alexander Ororbia. Contrastive-signal-dependent plasticity: Forward-forward learning of spiking neural systems. *arXiv preprint arXiv:2303.18187*, 2023.
- [7] Kashu Yamazaki, Viet-Khoa Vo-Ho, Darshan Bulsara, and Ngan Le. Spiking neural networks and their applications: A review. *Brain Sciences*, 12(7):863, 2022.
- [8] Larry F Abbott. Lapicque’s introduction of the integrate-and-fire model neuron (1907). *Brain Research Bulletin*, 50(5-6):303–304, 1999.
- [9] Wulfram Gerstner, Werner M Kistler, Richard Naud, and Liam Paninski. *Neuronal dynamics: From single neurons to networks and models of cognition*. Cambridge University Press, 2014.
- [10] Abhronil Sengupta, Yuting Ye, Robert Wang, Chiao Liu, and Kaushik Roy. Going deeper in spiking neural networks: VGG and residual architectures. *Frontiers in Neuroscience*, 13:95, 2019.
- [11] Seijoon Kim, Seongsik Park, Byunggook Na, and Sungroh Yoon. Spiking-yolo: spiking neural network for energy-efficient object detection. In *Proceedings of the AAAI Conference on Artificial Intelligence*, volume 34 (7), pages 11270–11277, 2020.
- [12] Rui-Jie Zhu, Qihang Zhao, and Jason K Eshraghian. Spikept: Generative pre-trained language model with spiking neural networks. *arXiv:2302.13939*, 2023.
- [13] Guangzhi Tang and Konstantinos P Michmizos. Gridbot: An autonomous robot controlled by a spiking neural network mimicking the brain’s navigational system. In *Proceedings of the International Conference on Neuromorphic Systems*, pages 1–8, 2018.
- [14] Emre O Neftci, Hesham Mostafa, and Friedemann Zenke. Surrogate gradient learning in spiking neural networks: Bringing the power of gradient-based optimization to spiking neural networks. *IEEE Signal Processing Magazine*, 36(6):51–63, 2019.
- [15] Nitish Srivastava, Geoffrey Hinton, Alex Krizhevsky, Ilya Sutskever, and Ruslan Salakhutdinov. Dropout: a simple way to prevent neural networks from overfitting. *The journal of machine learning research*, 15(1):1929–1958, 2014.
- [16] Anthony Zador, Sean Escola, Blake Richards, Bence Ölveczky, Yoshua Bengio, Kwabena Boahen, Matthew Botvinick, Dmitri Chklovskii, Anne Churchland, Claudia Clopath, et al. Toward next-generation artificial intelligence: Catalyzing the neuroai revolution. *arXiv:2210.08340*, 2022.
- [17] Heung-Chang Lee and Jeonggeun Song. Symba: Symmetric backpropagation-free contrastive learning with forward-forward algorithm for optimizing convergence. *arXiv:2303.08418*, 2023.
- [18] Guy Lorberbom, Itai Gat, Yossi Adi, Alexander Schwing, and Tamir Hazan. Layer collaboration in the forward-forward algorithm. In *Proceedings of the AAAI Conference on Artificial Intelligence*, volume 38, pages 14141–14148, 2024.
- [19] Yukun Yang. A theory for the sparsity emerged in the forward forward algorithm. *arXiv preprint arXiv:2311.05667*, 2023.
- [20] Guansong Pang, Chunhua Shen, Longbing Cao, and Anton Van Den Hengel. Deep learning for anomaly detection: A review. *ACM computing surveys (CSUR)*, 54(2):1–38, 2021.
- [21] Shiyu Liang, Yixuan Li, and Rayadurgam Srikant. Enhancing the reliability of out-of-distribution image detection in neural networks. *arXiv:1706.02690*, 2017.
- [22] Liron Bergman, Niv Cohen, and Yedid Hoshen. Deep nearest neighbor anomaly detection. *arXiv:2002.10445*, 2020.
- [23] Yiyu Sun, Yifei Ming, Xiaojin Zhu, and Yixuan Li. Out-of-distribution detection with deep nearest neighbors. In *International Conference on Machine Learning*, pages 20827–20840. PMLR, 2022.
- [24] Aitor Martinez-Seras, Javier Del Ser, Jesus L Lobo, Pablo Garcia-Bringas, and Nikola Kasabov. A novel out-of-distribution detection approach for spiking neural networks: Design, fusion, performance evaluation and explainability. *Information Fusion*, 100:101943, 2023.
- [25] Bolei Zhou, Aditya Khosla, Agata Lapedriza, Aude Oliva, and Antonio Torralba. Learning deep features for discriminative localization. In *IEEE Conference on Computer Vision and Pattern Recognition (CVPR)*, pages 2921–2929, 2016.
- [26] Ramprasaath R Selvaraju, Michael Cogswell, Abhishek Das, Ramakrishna Vedantam, Devi Parikh, and Dhruv Batra. Grad-cam: Visual explanations from deep networks via gradient-based localization. In *IEEE International Conference on Computer Vision (ICCV)*, pages 618–626, 2017.

- [27] Aditya Chattopadhyay, Anirban Sarkar, Prantik Howlader, and Vineeth N Balasubramanian. Grad-cam++: Generalized gradient-based visual explanations for deep convolutional networks. In *IEEE Winter Conference on Applications of Computer Vision (WACV)*, pages 839–847. IEEE, 2018.
- [28] Mohammed Bany Muhammad and Mohammed Yeasin. Eigen-cam: Class activation map using principal components. In *International Joint Conference on Neural Networks (IJCNN)*, pages 1–7. IEEE, 2020.
- [29] Youngeun Kim and Priyadarshini Panda. Visual explanations from spiking neural networks using inter-spike intervals. *Scientific Reports*, 11(1):19037, 2021.
- [30] Ammar Bitar, Rafael Rosales, and Michael Paulitsch. Gradient-based feature-attribution explainability methods for spiking neural networks. *Frontiers in Neuroscience*, 17, 2023.
- [31] Timothy P Lillicrap, Daniel Cownden, Douglas B Tweed, and Colin J Akerman. Random synaptic feedback weights support error backpropagation for deep learning. *Nature Communications*, 7(1):13276, 2016.
- [32] Jason K Eshraghian, Max Ward, Emre Neftci, Xinxin Wang, Gregor Lenz, Girish Dwivedi, Mohammed Benamoun, Doo Seok Jeong, and Wei D Lu. Training spiking neural networks using lessons from deep learning. *Proceedings of the IEEE*, 111(9):1016–1054, 2023.
- [33] Yann LeCun and Corinna Cortes. MNIST handwritten digit database. 2010.
- [34] Han Xiao, Kashif Rasul, and Roland Vollgraf. Fashion-mnist: a novel image dataset for benchmarking machine learning algorithms. *arXiv:1708.07747*, 2017.
- [35] Tarin Clanuwat, Mikel Bober-Irizar, Asanobu Kitamoto, Alex Lamb, Kazuaki Yamamoto, and David Ha. Deep learning for classical japanese literature. *arXiv:1812.01718*, 2018.
- [36] Gregory Cohen, Saeed Afshar, Jonathan Tapson, and Andre Van Schaik. Emnist: Extending mnist to handwritten letters. In *International Joint Conference on Neural Networks (IJCNN)*, pages 2921–2926. IEEE, 2017.
- [37] Yaroslav Bulatov. Notmnist dataset. *Google (Books/OCR), Tech. Rep.[Online]. Available: <http://yaroslavvb.blogspot.it/2011/09/notmnist-dataset.html>*, 2, 2011.
- [38] Brenden M Lake, Ruslan Salakhutdinov, and Joshua B Tenenbaum. Human-level concept learning through probabilistic program induction. *Science*, 350(6266):1332–1338, 2015.
- [39] Riccardo Scodellaro, Ajinkya Kulkarni, Frauke Alves, and Matthias Schröter. Training convolutional neural networks with the forward-forward algorithm. *arXiv preprint arXiv:2312.14924*, 2023.
- [40] Janez Demšar. Statistical comparisons of classifiers over multiple data sets. *The Journal of Machine Learning Research*, 7:1–30, 2006.
- [41] Alessio Benavoli, Giorgio Corani, Janez Demšar, and Marco Zaffalon. Time for a change: a tutorial for comparing multiple classifiers through bayesian analysis. *The Journal of Machine Learning Research*, 18(1):2653–2688, 2017.
- [42] Laurens Van der Maaten and Geoffrey Hinton. Visualizing data using t-sne. *Journal of Machine Learning Research*, 9(11), 2008.

A Reversal of Order in FF-SCP

This appendix formalizes the mathematical arguments that drive the reversal of the order in the scoring function. As pointed out in Subsection 3.2, the main limitation of the initial scoring function depicted in Equation (9) arises when, given a randomly selected sample from the ID dataset X , the following inequality holds:

$$\min_{c \in \mathcal{C}} d(\mathbf{0}, L_{c,c}) \leq \mathbb{E} \left[\min_{c \in \mathcal{C}} d(\mathcal{N}_1(X, c), L_{c,c}) \right]. \quad (12)$$

For instance, this reversal effect of the order predominantly occurs in OoD samples that were identified as negative inputs by the network, resulting in a near-zero latent state. Formally, let \mathcal{N} be an *accurate enough network*, defined as a network in which the following expression *almost always* holds:

$$\mathbb{E} \left[\|\mathcal{N}_1(\mathbf{X}_\ominus, c)\|_2 \right] < \epsilon, \quad (13)$$

where \mathbf{X}_\ominus denotes a random negative sample and ϵ represents a sufficiently low value. If this property holds, then we can understand the geometric behavior of $\mathcal{L}_{c,p}$, where p and c represent non-equal classes from \mathcal{C} .

Lemma A.1. *The discrete set $\mathcal{L}_{c,p}$, where c and p are distinct elements from \mathcal{C} , has a near-zero mean norm after the initial filtering step of the FF-SCP algorithm in accurate enough networks.*

Proof. Initial elements from $\mathcal{L}_{c,p}$ are predominantly composed of elements with a norm less than ϵ due to Equation (13), and, consequently, have a norm close to 0, with only a few elements having larger norms. After the highly active filtering step of the FF-SCP, it will be ensured that almost always the latent space $\mathcal{L}_{c,p}$ will be composed of elements with near-zero norm, and, as such, the fact that $\mathcal{L}_{c,p} \sim \mathbf{0}$ can be asserted. \square

Given an accurate enough network, in which a negative sample x_{\ominus} from an OoD distribution satisfies Equation (13), the scoring function can be simplified to:

$$s(x_{\ominus}) = \min_{p \in C} \sum_{c \in C} d(\mathcal{N}_1(x_{\ominus}, p), \mathcal{L}_{c,p}) \approx \min_{p \in C} \sum_{c \in C} d(\mathbf{0}, \mathcal{L}_{c,p}). \quad (14)$$

Additionally, since $d(\mathbf{0}, \mathcal{L}_{c,p}) \sim d(\mathbf{0}, \mathbf{0}) = 0$ when $p \neq c$, the expression can be further simplified to:

$$s(x_{\ominus}) = \min_{p \in C} \sum_{c \in C} d(\mathbf{0}, \mathcal{L}_{c,p}) \approx \min_{p \in C} d(\mathbf{0}, \mathcal{L}_{p,p}). \quad (15)$$

This implies that for an OoD sample that remains with near-zero norms for all candidate embedded labels, the value of $s(x_{\ominus})$ will be approximately equal to the distance between the zero vector and the closest point among all the latent clusters $\mathcal{L}_{p,p}$, where $p \in C$.

Similarly, given the same network \mathcal{N} and an ID sample x_{\oplus} , the scoring function $s(x_{\oplus})$ can be simplified for negative samples. Using Equation (13) and applying the same logic as with the OoD samples, the summation over the different latent clusters can be reduced to only the value of the latent cluster forwarded to the real label, i.e.:

$$s(x_{\oplus}) = \min_{p \in C} \sum_{c \in C} d(\mathcal{N}_1(x_{\oplus}, p), \mathcal{L}_{c,p}) \approx \min_{p \in C} d(\mathcal{N}_1(x_{\oplus}, p), \mathcal{L}_{p,p}), \quad (16)$$

which implies that $s(x_{\oplus})$ is approximated by the minimal distance between the latent vector of x_{\oplus} and the closest latent point in L_p^p . If the distance between points inside the cluster is sufficiently large, to the extent where it surpasses the value $\min_{p \in C} d(\mathbf{0}, \mathcal{L}_{p,p})$, the value of $s(x_{\oplus})$ will be greater than $s(\ominus)$. The distance inside the latent clusters can become large due to several reasons, including the curse of dimensionality, insufficient sampling points for the latent clusters, and the tendency of FFA to push high activity points away from the zero vector, creating cluster spaces with a large diameter. While increasing the number of samples for the latent representation can enhance the distance accuracy, it comes at the expense of increased computational requirements.

B Latent State of FFA

This appendix offers additional insights into the structure of the latent activity of networks trained using the FFA and the enhanced representational capabilities it provides. To analyze this space, we rely on the trained models used for the OoD detection experiments, specifically the analog model using ReLU activation functions and the bounded goodness SNN. These two models have been selected as they encompass both activity regimes observed during the experimentation: the sparse latent space and the bounded latent space. To avoid redundancy in the latent space, and given the similar latent behavior arising from the different datasets, we employ random batches of data from the MNIST dataset to extract the latent spaces.

The plot showing the latent vectors obtained from the analog ReLU network is depicted in Figure 8. Consistent with the findings of Tosato et al. [4] and Yang [19], the latent vectors emerging from these networks are characterized by sparse activity regimes and high neural specialization. As observed in the images, most latent vectors are composed of only a small subset of active neurons, which represent key distinctive features of the different classes. For instance, given that the latent vectors of the images are ordered by class, it can be observed that the set of neurons that activate when presented with each input distribution is highly consistent among the batch. Similarly, each neuron is usually only active when presented with a small subset of the available input classes, often being active with only one.

Similarly, Figure 9 shows the latent activity from the network trained using FFA with the $G_0(\cdot)$ goodness function. In contrast to the previous network, the representations obtained showcase a denser activity regime, with latent vectors comprising a larger set of active neurons per instance. As in the previous case, the activity of the data follows class-based activation patterns, with each neuron specializing in a specific set of classes. However, in this instance, the set of active classes results in a broader selection, allowing for more classes to activate each neuron. Upon early experimentation, the emergence of these representations appears to be a byproduct of the bounded regimes of the goodness functions. Due to the inability to achieve unbounded goodness through a small set of unbound neurons, the network relies on a larger set of neurons for each sample. In contrast with the unbounded models, where the negative samples resulted in

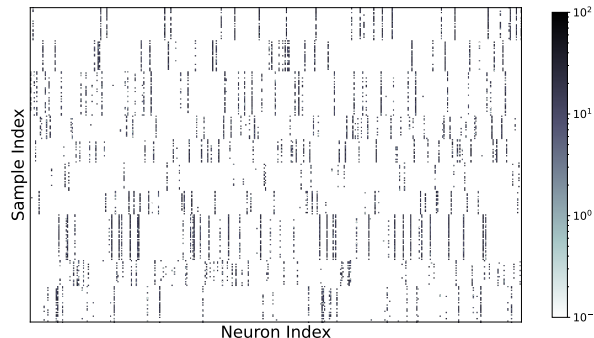


Figure 8: Latent vector of the first layer of 256 random samples extracted from a ReLU activated network trained with FFA. Only the first 400 neurons are displayed. The samples are ordered by class.

near-zero latent vectors, bounded models persist in the increased latent activity, resulting in negative latent vectors that contain a positive-like structure but within lower activity regimes. While the results in Table 1 indicate a small decrease in the accuracy of these networks, the increased bound of activity yields positive outcomes in terms of representability, as shown in the OoD detection results in Table 2.

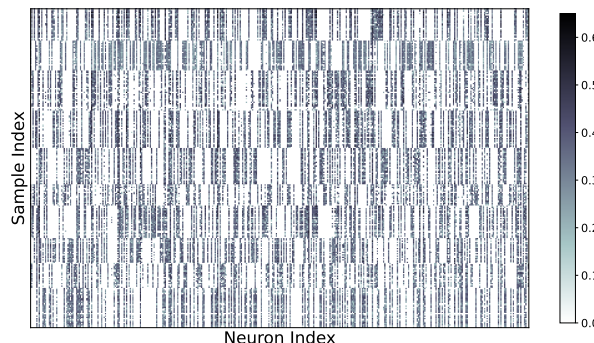


Figure 9: Latent vector of the first layer of 256 random samples extracted from the SNN using $G_0(\cdot)$. Only the first 400 neurons are displayed. The samples are ordered by class.

To provide a more in-depth analysis of the geometrical properties of these latent vectors, we employed dimensionality reduction methods to present approximate depictions of the structure of the latent space. We relied on the T-SNE algorithm [42], using 1024 randomly chosen samples from MNIST, with latent vectors obtained by using all 10 available class labels. This approach allows us to explore the geometrical relationship between positive and negative samples, beyond the activity differences.

The latent space of the analog networks is depicted in Figure 10. Once again, our results align with those observed by other researchers: positive samples cluster together, farther from the zero vector, and are highly separated from negative samples. Similarly, the position of the negative set also appears to contain a clearly defined structure, with most samples staying close to the origin. It’s important to note that T-SNE is known to exhibit a partially distorted projection of the space, where distances do not necessarily represent exact mappings to the higher-dimensional original space. As such, our assertion on the closeness of negative samples to the origin of the space has been further analyzed manually by verifying their activity magnitude distribution. This analysis confirms that negative samples showcase lower latent activities, and instances farther from zero are still closer to zero than their positive counterparts.

Conversely, Figure 11 illustrates the space obtained by employing the spiking network with bounded goodness. One clear property that arises as a consequence of the denser latent activity is the higher clustering of the negative latent vectors into smaller subclusters. These subclusters correspond to samples obtained from pairs of real classes and embedded labels, showing how the algorithm discerns between different class selections based on their arguments. This latent geometry offers more precise results when measuring distances to OoD samples, as the clusters of class/label representatives provide closer distances among samples from the same distribution. This results in a more distinct separation between positive and negative samples in the space. However, this geometric property does not necessarily

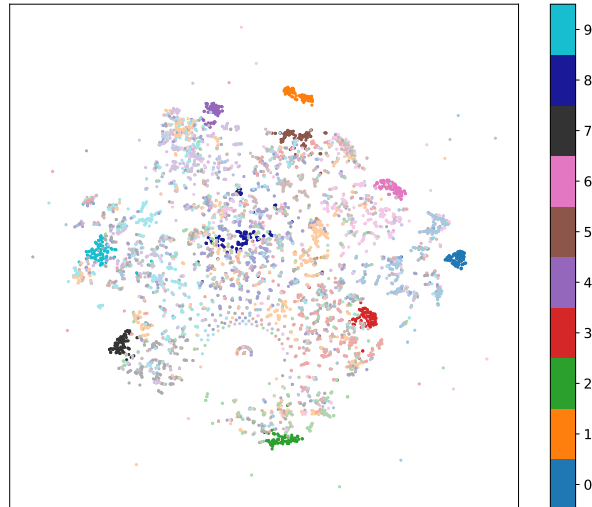


Figure 10: T-SNE projection of the latent vectors from the first layer of the analog neural network. The latent space includes 1024 random samples from MNIST, incorporating both positive and negative labels. Positive latent vectors are illustrated using darker colors to differentiate them from negative samples.

translate to enhanced accuracy, as the denser latent vectors and higher separation also reduce the specialization of neurons in the layer.

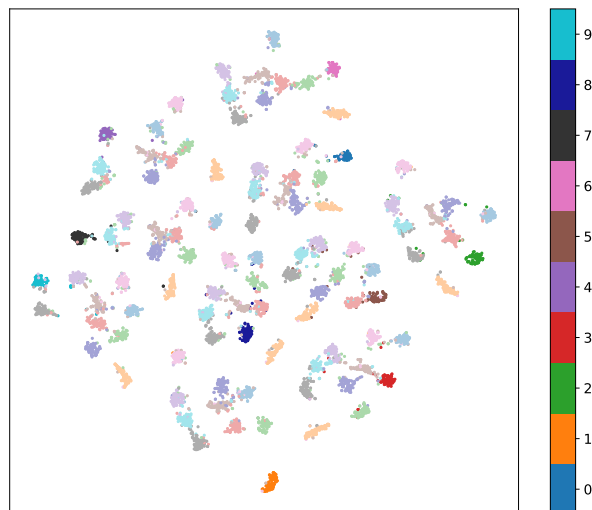


Figure 11: T-SNE projection of the latent vectors from the first layer of the spiking neural network. The latent space includes 1024 random samples from MNIST, incorporating both positive and negative labels. Positive latent vectors are illustrated using darker colors to differentiate them from negative samples.

C OoD Detection Results without Order Reversal Considerations

This appendix presents the results obtained when employing the FF-SCP algorithm when employing the $s(\cdot)$ scoring function. As previously mention in Section 3.2, the function $s(\cdot)$ does not properly measure the distance in scenarios where the intra-cluster distance is greater than the distance between the zero vector and each sample of positive latent clusters, which is formally proven in Appendix A. As expected, the results from Table 3 evidence the reduced OoD detection accuracy when compared to the ones from Table 2, which relies on the refined scoring function $S(\cdot)$.

Table 3: Results of the FF-SCP algorithm using the $s(\cdot)$ of our three proposed networks: the Analog FF-Network; the Unbounded FF-Network, denoted as $G_\infty(\cdot)$; and the Bounded FF-Network, denoted as $G_0(\cdot)$. Data from the SCP and ODIN has been extracted from the paper [24]. The ANN results are only shown as a baseline to compare ANN vs SNN.

ID Dataset	OOD Dataset	AUROC \uparrow					AUPR \uparrow					FPR95 \downarrow				
		FF-SCP Analog	FF-SCP $G_\infty(\cdot)$	FF-SCP $G_0(\cdot)$	SCP	ODIN	FF-SCP Analog	FF-SCP $G_\infty(\cdot)$	FF-SCP $G_0(\cdot)$	SCP	ODIN	FF-SCP Analog	FF-SCP $G_\infty(\cdot)$	FF-SCP $G_0(\cdot)$	SCP	ODIN
MNIST	Omniglot	83.19	90.25	88.80	71.56	94.72	89.24	92.19	91.67	71.90	94.28	50.28	29.65	36.03	88.93	29.08
	notMNIST	99.99	99.98	99.98	99.14	64.45	99.99	99.99	99.99	99.01	57.16	0.00	0.00	0.00	03.60	86.65
	FMNIST	93.04	97.88	99.37	91.21	73.97	94.62	97.73	99.40	87.15	65.29	50.28	11.22	3.38	24.95	77.11
	KMNIST	97.87	98.39	99.40	94.89	73.97	98.12	98.38	99.42	94.92	76.27	13.49	8.92	3.39	24.99	72.87
	Letters	84.80	91.26	96.88	88.11	81.43	92.46	95.55	98.48	79.49	64.19	61.61	42.22	15.25	51.66	73.89
FMNIST	MNIST	99.07	99.03	98.59	92.60	95.98	98.72	98.42	97.99	93.18	95.74	3.65	3.27	5.04	35.48	17.37
	Omniglot	98.83	98.72	95.46	84.75	97.86	99.09	98.78	96.76	85.37	97.83	4.72	4.09	21.08	63.55	09.97
	notMNIST	99.85	99.93	99.92	98.87	61.70	99.93	99.96	99.96	99.14	61.75	0.10	0.07	0.27	02.47	92.33
	KMNIST	97.27	97.83	98.10	84.56	88.36	97.13	97.48	97.86	82.41	88.84	13.34	9.46	8.75	53.10	57.39
	Letters	97.80	98.32	97.11	92.83	91.83	98.72	98.84	98.51	88.10	85.15	10.13	7.05	16.06	34.49	39.82
KMNIIST	MNIST	87.35	87.36	61.13	61.85	85.79	80.92	82.12	53.79	61.64	88.57	36.55	41.84	75.55	89.34	51.64
	Omniglot	85.68	82.28	54.87	58.54	96.43	88.94	85.73	62.51	59.68	97.25	47.07	51.68	69.27	92.58	08.09
	notMNIST	92.79	95.74	99.08	96.88	67.24	96.88	98.04	99.50	96.68	67.59	60.16	34.05	3.94	09.52	81.37
	FMNIST	17.92	32.95	66.42	75.00	76.73	33.85	39.38	59.32	72.85	78.58	97.96	96.78	72.01	66.14	70.67
	Letters	71.46	80.69	81.66	78.34	85.14	79.16	85.23	83.94	64.47	80.65	65.63	51.44	46.22	71.49	53.51
Letters	MNIST	87.64	83.26	83.65	69.06	80.98	80.61	76.33	71.52	82.30	88.73	53.65	71.52	68.37	88.83	68.13
	Omniglot	79.73	81.14	85.28	77.60	97.11	77.35	76.11	77.66	88.04	98.54	68.44	59.40	40.72	87.11	15.54
	notMNIST	99.98	99.99	99.95	98.63	58.08	99.98	99.99	99.95	98.90	69.65	0.00	0.00	0.00	07.48	93.94
	FMNIST	90.09	95.98	91.01	86.33	71.30	88.94	94.88	84.47	92.08	83.66	70.62	27.30	35.04	47.30	88.04
	KMNIST	99.21	99.65	97.27	86.31	77.60	98.63	99.35	95.21	92.15	85.47	3.83	1.42	14.93	51.41	77.88
	Average	88.18	90.53	89.70	84.35	81.03	89.66	90.72	88.40	84.47	81.25	35.58	27.57	26.76	49.72	58.26
	Median	92.91	96.90	97.00	86.32	81.20	95.75	97.61	97.31	87.59	84.40	41.81	19.26	15.65	51.53	69.4